applied sciences

MDPI

Article

Mission-Gilded Baroque Terracotta Sculptures by Lorenzo Vaccaro: A Multi-Analytical Investigation of Materials and Degradation

Andrea Macchia [1,*], Laura Palermo [1,2], Camilla Zaratti [1,3], Irene Angela Colasanti [1,3], Federica Valentini [2] and Tilde de Caro [4,*]

[1] YOCOCU APS (YOuth in COnservation of CUltural Heritage), Via Torquato Tasso 108, 00185 Roma, Italy; laurapalermo1999@gmail.com (L.P.); camilla.zaratti@students.uniroma2.eu (C.Z.); ireneangela.colasanti@students.uniroma2.eu (I.A.C.)
[2] Accademia di Belle Arti di Napoli, Via S. Maria di Costantinopoli 107, 80138 Naples, Italy; federica.valentini@uniroma2.it
[3] Sciences and Chemical Technologies Department, Tor Vergata University, Via della Ricerca Scientifica 1, 00133 Rome, Italy
[4] Institute of Nanostructured Materials—National Research Council (ISMN-CNR), Strada Provinciale 35d, n.9, 00010 Montelibretti, Italy
* Correspondence: aps@yococu.com (A.M.); tilde.decaro@cnr.it (T.d.C.)

Abstract

This study presents a multi-analytical investigation of two Baroque gilded terracotta sculptures—*Hercules and the Nemean Lion* (Hercules A) and *Hercules and the Lernaean Hydra* (Hercules B)—attributed to Lorenzo Vaccaro (1655–1706) and preserved at the Museo Civico Gaetano Filangieri in Naples. This research aimed to reconstruct the original manufacturing technique, characterize materials introduced by successive restoration interventions, and identify active degradation mechanisms. A systematic diagnostic approach integrating UV fluorescence imaging, digital optical microscopy, portable energy-dispersive X-ray fluorescence spectroscopy (EDXRF), Raman spectroscopy, Fourier-transform infrared spectroscopy in attenuated total reflectance mode (FTIR-ATR), scanning electron microscopy with energy-dispersive X-ray spectroscopy (SEM-EDS), and spectrocolorimetry was applied. The original gilding system—comprising a ferruginous silico-aluminous terracotta substrate, a calcium sulfate ground, a lead-white *imprimitura*, an iron-rich bole, and a thin gold leaf—is consistent with documented Baroque mission gilding practices in Southern Italy. Analytical evidence further documented extensive non-original interventions, including copper-based artificial patination, bronze powder (*porporina*) integration, poly (vinyl acetate) adhesives, and acrylic protective coatings. Raman spectroscopy identified the in situ conversion of intentionally applied tenorite (CuO) to malachite ($Cu_2CO_3(OH)_2$) as an active degradation pathway. Spectrocolorimetric measurements quantified chromatic alterations of up to $\Delta E = 52$ attributable to accumulated surface deposits. The proposed integrated methodology constitutes a replicable diagnostic framework for investigating gilded terracotta artefacts in museum collections.

Keywords: gilding; multi-analytical investigation; degradation mechanisms

Check for updates

Academic Editors: Graça Vasconcelos and Amélia Dionísio

Received: 7 April 2026
Revised: 3 May 2026
Accepted: 11 May 2026
Published: 13 May 2026

Copyright: © 2026 by the authors. Licensee MDPI, Basel, Switzerland. This article is an open access article distributed under the terms and conditions of the Creative Commons Attribution (CC BY) license.

1. Introduction

The scientific characterization of the materials constituting historical artworks has established itself as one of the central concerns of modern heritage science, providing a

rigorous empirical foundation for art-historical interpretation, technological reconstruction, and conservation planning [1–3]. Determining which substances were employed by artists and craftsmen, encompassing ground preparations, pigments, binding media, metallic components, and surface finishes, yields data that neither visual examination nor archival documentation alone can supply [4–8]. Beyond their diagnostic value, the results of such investigations are equally essential for tracing the geographical and chronological transmission of craft practices across historical periods and production centers, and for designing conservation interventions that are chemically and physically compatible with the original material fabric of the object under study [9–11].

Gilded ceramic artefacts occupy a technically and historically distinctive place within this field of inquiry. The application of gold leaf over a terracotta substrate generates a multilayered system in which materials with fundamentally different physical and chemical properties are brought into direct contact: a porous, thermally sensitive ceramic body and a thin, mechanically fragile metallic surface [12,13]. This structural condition makes gilded terracotta particularly vulnerable to degradation driven by environmental fluctuations, mechanical stress, and the cumulative effects of historical use and handling [14,15]. The conservation challenges inherent to such objects are compounded when successive restoration campaigns have introduced additional, heterogeneous materials, including metallic powders, synthetic resins, adhesives, and surface coatings, whose properties may be incompatible with the original stratigraphy, creating further pathways for deterioration [16].

Southern Italian Baroque terracotta sculpture represents a historically significant yet analytically underexplored instance of this class of objects. Despite the recognized artistic importance of Neapolitan Baroque sculptural production, systematic scientific data on the material composition of gilded terracottas from this period and region remain scarce. Existing analytical studies on gilded artworks have tended to address either the technology of original gilding systems [17–26] or the characterization of restoration materials [27–33] as separate questions, without confronting the stratigraphic complexity that arises when the two are superimposed. This gap has direct consequences for conservation practice: in the absence of a clear material map distinguishing original layers from later additions, selective and reversible intervention is difficult to plan and execute.

The present study focuses on two Baroque gilded terracotta sculptures attributed to Lorenzo Vaccaro (1655–1706): Hercules and the Nemean Lion (hereafter Hercules A; 55 × 38 × 22 cm, height × width × depth), and Hercules and the Lernaean Hydra (hereafter Hercules B; 60 × 33 × 28 cm, height × width × depth) [34], preserved at the Museo Civico Gaetano Filangieri in Naples [35,36]. These works are among the rare extant examples of mission-gilded terracotta from the Neapolitan Baroque context. Their attribution history reflects the broader difficulties inherent in the study of this class of objects: initially assigned to Giuseppe Sanmartino, then to an unknown author, the sculptures were attributed to Lorenzo Vaccaro in 1970 by Gennaro Borrelli on stylistic grounds. In 2015, Paola D'Agostino proposed a connection with the patronage of the viceroy Gaspar de Haro y Guzmán, Marquis del Carpio, and a possible intended destination as models for metal casting, placing their execution between 1683 and 1687 [37,38]. A 1745 inventory lists among the property of Domenico Antonio Vaccaro two gilded statuettes representing Hercules and Samson, raising the possibility that the sculptures remained in the Vaccaro workshop after the death of the patron [39]. The gilding itself, concealed beneath a thick layer of artificial bronze patination, was rediscovered only in 1978, on the occasion of the exhibition Civiltà del '700 a Napoli [40]. A Soprintendenza document dated 1986 subsequently recorded the precarious conservation condition of statues, which had suffered further structural damage during the 1980 earthquake. A restoration campaign conducted between 1980 and 1986, carried out in emergency conditions, introduced calcium carbonate fills, bronze powder

integrations (*porporina*), and synthetic adhesives, the compatibility and long-term stability of which required systematic analytical assessment.

Against this historical background, the present study reconstructs the material stratigraphy of two Baroque mission-gilded terracotta sculptures attributed to Lorenzo Vaccaro through an integrated multi-analytical investigation with the objectives of discriminating the original gilding system from materials introduced by successive restoration campaigns and of identifying the degradation mechanisms currently active on their surfaces.

2. Materials and Methods

The analytical approach employed a systematic sequence from non-invasive surface documentation to targeted micro-sampling for compositional analysis. Surface documentation preceded all invasive procedures to identify areas of interest and guide subsequent instrumental investigations. UV fluorescence photography and digital microscopy were used to provide initial surface characterization and to guide the selection of sampling points for XRF mapping and micro-sampling. All measurements adhered to standard operating procedures for cultural heritage analysis, with particular attention to minimize sampling and surface impact (following EN 16085:2012 [41]; EN 16853:2017 [42]). Analytical sequences were documented photographically to enable correlation between instrumental data and surface locations.

2.1. Non-Invasive Surface Characterization

Ultraviolet Fluorescence Photography was performed using a Canon M50 camera, modified for full spectrum acquisition (EOS M50, Canon, Tokyo, Japan) with 365 nm LED illumination (30 W). Images were captured with a UV filter and combined with yellow/UV filter configurations to enhance contrast and identify fluorescent materials. This technique enables the detection of organic compounds, including varnishes, adhesives, and restoration materials not visible under standard lighting conditions [43–45]. Optical Microscopy employed a DinoLite AM411-FVW microscope (AnMo Electronics Corp., New Taipei City, Taiwan) at 80× magnification under visible illumination. Surface morphology documentation included identification of microfractures, layer discontinuities, and material remnants [46]. Microscopic examination guided the selection of sampling points for subsequent instrumental analysis, particularly directing XRF measurements toward areas exhibiting distinct surface characteristics and potential material variations.

Energy dispersive X-ray fluorescence spectroscopy (EDXRF, instrument model Hitachi MET 3600, Tokyo, Japan) provided elemental composition mapping across sculpture surfaces. The instrument operates with a rhodium-target X-ray tube (4 W, 30 kV maximum, 200 μA maximum current) and a silicon drift detector (140 eV resolution at 100 kcps). The standard analysis spot area measured 10.7 × 9.4 mm^2 and could be expanded to 25 mm^2 for irregular surfaces. The EDXRF system setting enabled the detection of light elements such as Si, S, and Mg, which are relevant for ceramic and gilding characterization, as well as heavy metals such as Au, Pb, indicative of the gilding technique [47]. EDXRF measurement areas were assigned to material categories—ceramic body, black patina, green patina, original gilding, *gesso/biacca* layer, simulated gilding (*porporina*), and other—based on their macroscopic visual appearance, as assessed by prior UV fluorescence imaging and optical microscopy. These assignments represent interpretive classifications guided by surface morphology.

Spectrocolorimetric analysis was performed on selected surface areas to provide a quantitative characterization of the chromatic properties of the different material categories identified on the sculptures, including areas of original gilding, exposed bole, artificial patination, and bronze powder (*porporina*) integrations. Measurements were acquired

using a YS3010 3nh handheld spectrophotometer (Shenzhen ThreeNH Technology Co., Ltd., Shenzhen, China). Colorimetric coordinates L*, a*, and b* were recorded in the CIE Lab* color space, and the total color difference ΔE*ab was calculated between pairs of measurements acquired on areas with contrasting surface conditions. ΔE values below 5 are generally considered below the threshold of visual perceptibility [48,49].

2.2. Micro-Sampling and Compositional Analysis

Micro-sampling was carried out to enable compositional characterization of the gilding stratigraphy, surface patinas, and materials associated with degradation and restoration interventions. The selection of sampling locations was based on the preliminary results of UV fluorescence imaging, optical microscopy, and EDXRF analysis, which identified areas of diagnostic interest characterized by distinct surface conditions: preserved original gilding, exposed ground layers, copper-based patination, bronze powder deposits, and synthetic adhesive residues. This integrated pre-sampling survey ensured that the collected specimens were representative of the principal material categories present on both sculptures.

Sample extraction was performed mechanically using a fine tungsten-carbide scalpel under stereomicroscopic control, limiting removal to the minimum quantity required for analysis. Sampling was restricted to areas already exhibiting physical compromise, including zones of gilding loss, delamination, and surface lacunae, in order to avoid further damage to intact original surfaces. A total of eight micro-samples were collected for FTIR-ATR analysis and three for SEM-EDS cross-sectional examination [50]. The distribution of sampling points across both sculptures is shown in Figures 1 and 2; the material category targeted at each location is summarized in Table 1.



Figure 1. Hercules A, sampling points, and diagnostic investigation areas (XRF analysis spot in black; FTIR in red; in green spot of sample collected for Raman analysis).

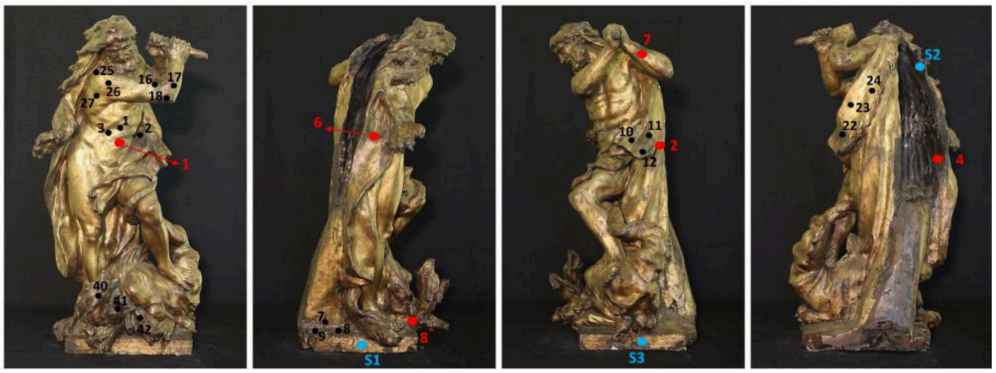

Figure 2. Hercules B, sampling points, and diagnostic investigation areas (XRF analysis spot in black; FTIR in red; in blue spot of sample collected for SEM analysis).

Table 1. Sampling points and analytical techniques (EDXRF excluded).

Sample/Analysis ID	Anatomical Location	Technique	Material Category	Hercules
Sample 1	Torso	FTIR-ATR	*Porporina* powder	B
Sample 2	Left drapery	FTIR-ATR	Brown-dark patina on gilding	B
Sample 3	Lion's thigh	FTIR-ATR	Brown-dark patina on gilding	A
Sample 4	Back, ungilded area	FTIR-ATR	Black patina	B
Sample 5	Hidden drapery area	FTIR-ATR	Black patina	A
Sample 6	Surface crack area	FTIR-ATR	Glue (PVAc)	B
Sample 7	Arm	FTIR-ATR	Glue (PVAc)	B
Sample 8	Base	FTIR-ATR	Synthetic protective coating	B
Fragment 1 (S1)	Base, right side	SEM-EDS	Stratigraphic cross-section	A
Fragment 2 (S2)	Lion skin, back	SEM-EDS	Stratigraphic cross-section	B
Fragment 3 (S3)	Base, left side	SEM-EDS	Stratigraphic cross-section	B

Raman spectroscopy was performed using a portable Raman spectrometer (model RK785-I, Oceanhood, Shanghai, China) equipped with a 785 nm laser excitation wavelength and a spectral resolution of 4 cm^{-1}. Analyses were targeted on greenish and dark surface residues previously identified by optical microscopy and EDXRF, particularly in areas associated with copper-based patination and metallic surface treatments. Laser power was varied in the range 0.5–150 mW, depending on the optical response and sensitivity of each sample, in order to optimize signal quality while minimizing the risk of thermal damage to the surface. Spectra were acquired with 3 accumulations of 5 s each (total acquisition time 15 s per spectrum). Spectral interpretation was supported by comparison with published reference databases for copper corrosion products and inorganic pigments. The acquired spectra exhibited a pronounced fluorescence background, consistent with the fluorescence interference associated with patinas containing organic compounds. Spectra were pre-processed by fluorescence background subtraction and baseline correction; no smoothing or band reconstruction was applied.

Fourier-transform infrared spectroscopy in attenuated total reflectance mode (FTIR-ATR) was carried out using a Thermo Scientific Nicolet Summit PRO spectrometer (Thermo Fisher Scientific, Waltham, MA, USA) equipped with an Everest™ diamond ATR crystal accessory. Spectra were acquired over the range 4000–600 cm^{-1} at a spectral resolution of 8 cm^{-1} with 32 scans per measure. Micro-samples were placed in direct contact with the ATR crystal without further preparation. Spectral assignment was supported by comparison with instrumental library databases and published reference spectra for organic binders, synthetic polymers, and inorganic compounds relevant to gilded heritage objects [32].

Scanning electron microscopy with energy-dispersive X-ray spectroscopy (SEM-EDS) was performed using a Tescan VEGA3 scanning electron microscope (Brno, Czech Republic) coupled with an X-ray spectroscopy system (INCA 2000, Oxford Instruments, Abingdon, UK). Before analysis, micro-samples were embedded in epoxy resin and prepared as polished cross-sections. Analyses were conducted in high-vacuum mode using a 30 keV accelerating voltage and backscattered electron (BSE) detection, which provides compositional contrast proportional to mean atomic number and allows for clear differentiation between stratigraphic layers of differing composition. Imaging magnifications ranged from 260× to 1100×. EDS point analyses were performed on selected regions of interest to determine the elemental composition of individual layers.

3. Results

3.1. Multispectral Imaging Analysis

UV fluorescence examination revealed heterogeneous optical responses across the surfaces of both sculptures, characterized by distinct zones of UV absorption and selective reflectance rather than intense fluorescence phenomena. In areas where the gilding had been partially lost, exposed white preparatory layers exhibited a yellowish fluorescence under UV illumination. While this behavior may be consistent with the presence of zinc-based compounds in the ground layer, UV-induced fluorescence alone is not sufficient for definitive identification and must be validated by complementary analytical techniques [51].

The most diagnostically significant contrast was observed between zones displaying intense reflection of the blue component of the UV source and adjacent areas of markedly attenuated reflectance. The UV-absorbing zones correspond to surfaces covered by a non-fluorescent material that effectively masks the optical response of the underlying gilded layers. This attenuation pattern was not uniformly distributed: it was particularly pronounced on the frontal and lateral surfaces of both sculptures, while the posterior areas showed significantly less UV absorption. The spatially selective distribution of this phenomenon, concentrated on the most visually prominent surfaces, suggests an intentional application rather than uniform environmental deposition.

The UV-absorbing material occurs as irregularly distributed layers of variable thickness and coverage rather than as a continuous film. The complete absence of fluorescence is consistent with the presence of UV-absorbing compounds, which may include non-fluorescent organic substances such as bituminous materials, oxidized waxes, or hydrocarbon-based compounds, as well as inorganic phases such as metal oxides or mineral pigments [52]. Taken together, the spatial distribution and optical behavior of these surface layers are consistent with a deliberately applied patination treatment intended to modify the perceived surface finish of both sculptures.

Figure 3 shows the images taken in visible light, UV light, and UV with a yellow filter, from the frontal view. The UV fluorescence response indicates a non-fluorescent, UV-absorbing surface layer preferentially distributed on the frontal and lateral surfaces of both sculptures. Its chemical composition was investigated by the spectroscopic and microanalytical techniques described below.

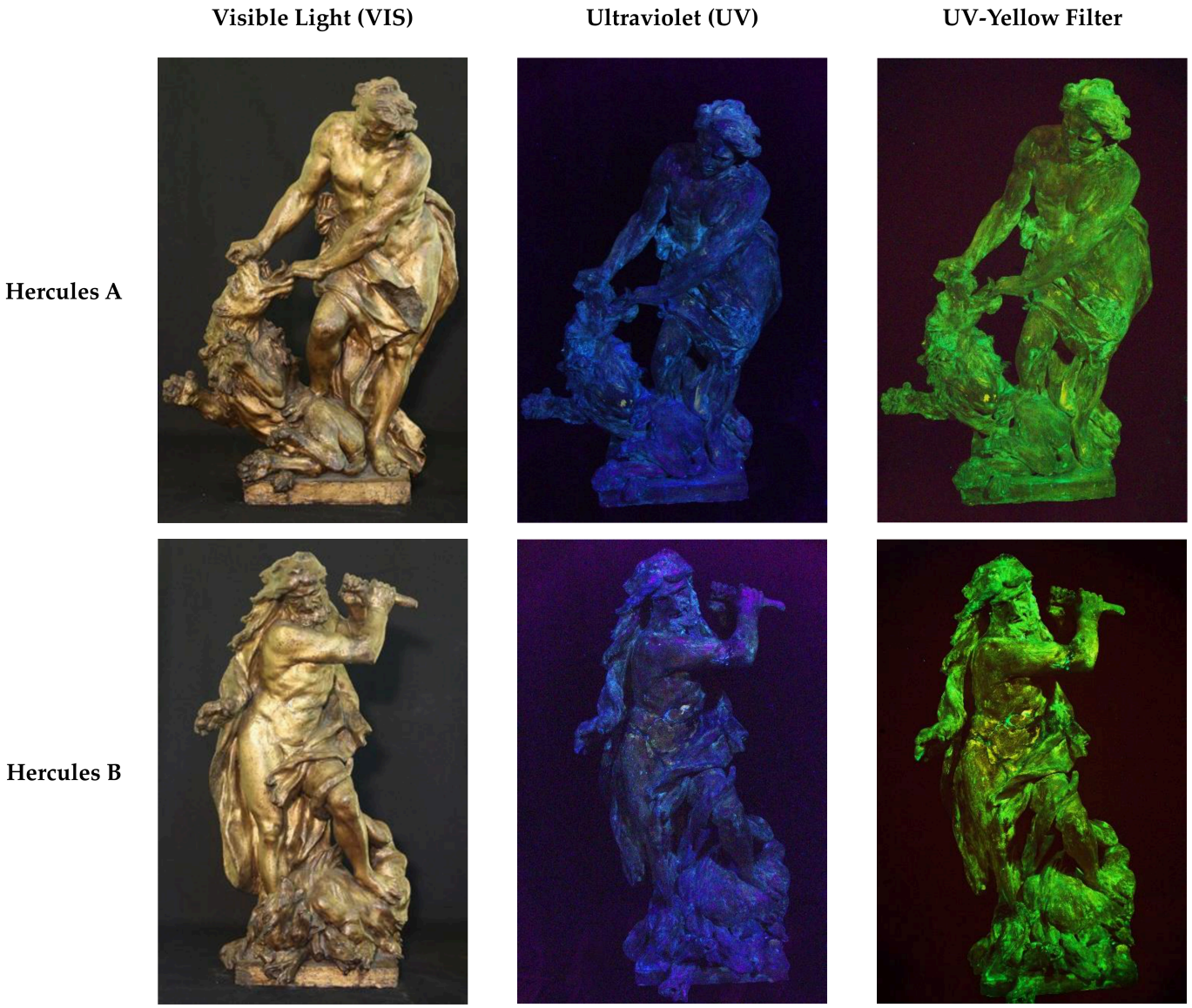

Figure 3. The images show the sculpture surface under VIS, UV fluorescence, and UV with filter fluorescence, highlighting areas with a distinct response compared to the surrounding material, suggesting retouching or overpainting. Images of the sculpture surface under VIS, UV fluorescence, and UV with filter fluorescence.

3.2. Optical Microscopy Observation

Digital optical microscopy at 80× magnification under visible light revealed complex surface morphologies resulting from the superimposition of original materials, degradation products, and multiple restoration interventions. In areas of gilding loss, a well-defined stratigraphic sequence was documented, consisting of residual gold leaf overlying a reddish bole layer; in zones of more advanced loss, this sequence was further underlain by a compact, homogeneous white preparatory layer. This layered arrangement is consistent with mission gilding techniques applied to terracotta substrates. Where material loss was most extensive, the exposed ceramic substrate exhibited a fine-grained texture with scattered mineral inclusions.

Extensive microcrack networks were documented across both sculptures, particularly concentrated on convex surfaces and in areas of elevated mechanical stress, including the limbs and musculature (Figure 4a). The fracture morphology varies systematically: fine, irregular networks with random orientation are consistent with thermal stress and long-term material aging, while linear fractures following anatomical contours suggest mechanical impact or handling damage. Radial crack systems emanating from discrete points indicate localized pressure- or impact-induced damage, and parallel crack systems aligned with the underlying ceramic grain structure reflect differential dimensional changes between substrate and surface layers (Figure 4b).

Residual metallic powders with a characteristic golden-bronze tonality were documented throughout both sculptures, particularly concentrated in recessed or partially sheltered areas. These granular deposits exhibit a dull, oxidized appearance consistent with bronze powder (*porporina*) applications used to reintegrate losses in the original gilding during historical restoration campaigns (Figure 4c). Documentary evidence places this intervention between 1980 and 1986; photographic documentation from the Tumidei archive dated 1996 records the progressive darkening of these powders within approximately 10–15 years of application. At the interface between the bronze powder deposits and the original gilding, greenish surface residues were frequently observed, embedded within microcracks and along the boundary between surviving gold and exposed ground layers. These deposits are consistent with copper-based corrosion products generated by the oxidation of the restoration material (Figure 4d).

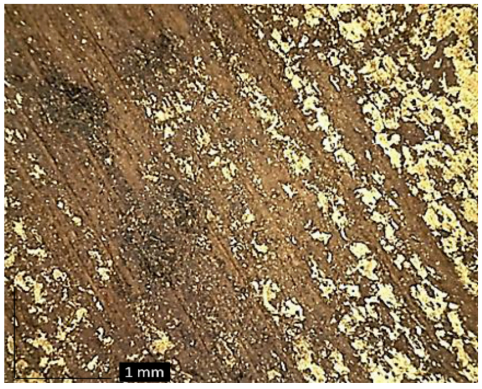

(**a**) Partial delamination

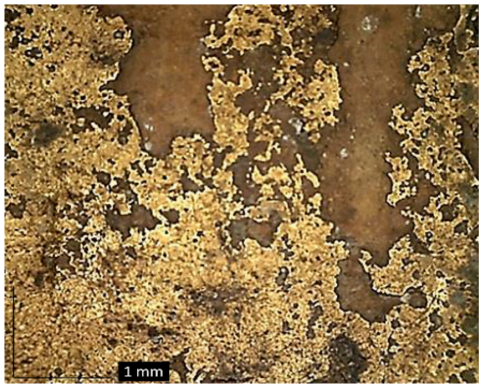

(**b**) Gilding losses and cracks

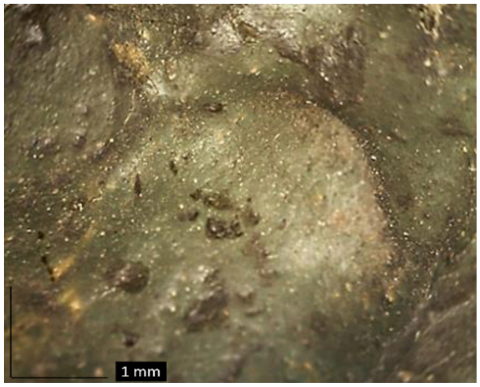

(**c**) Simulated bronze patina

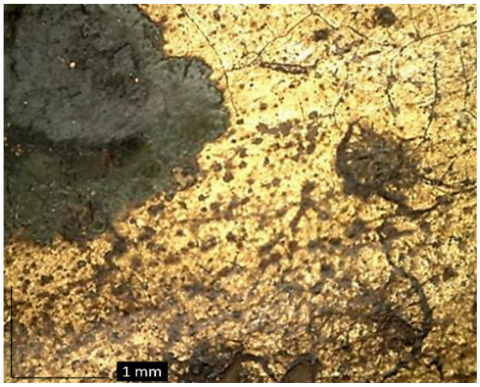

(**d**) Crack patter and patina remnants

Figure 4. *Cont*.

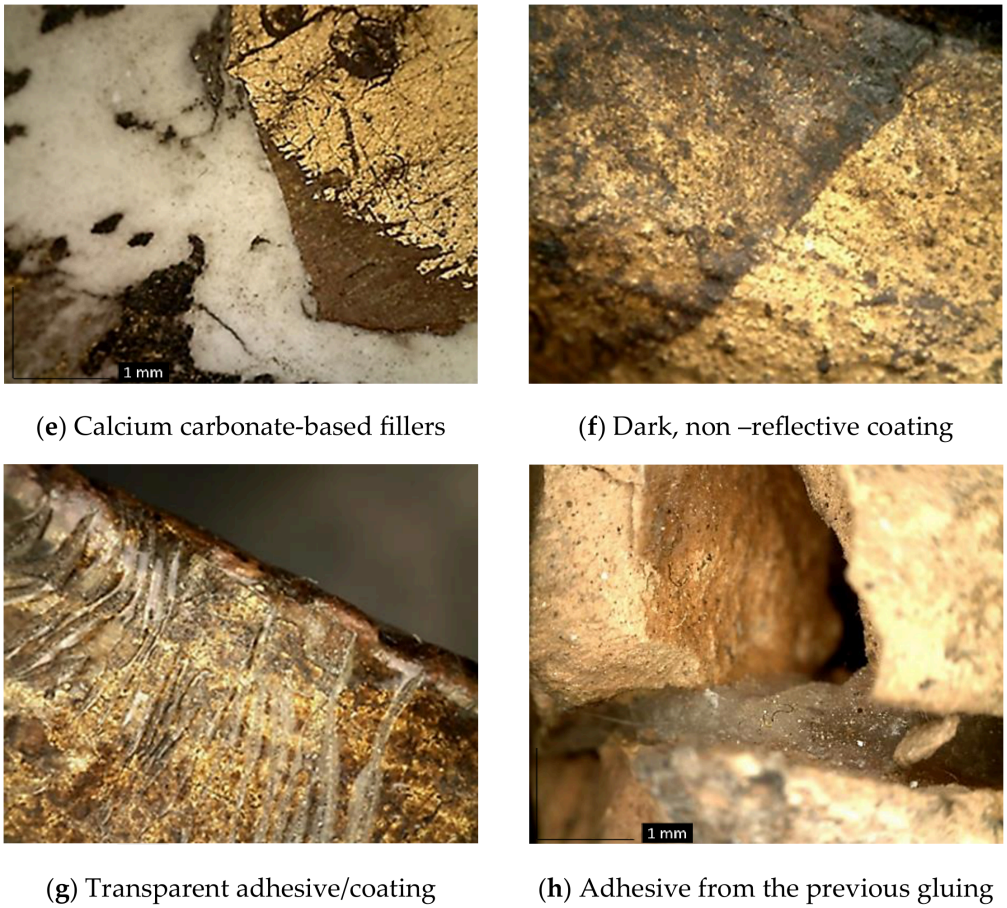

(**e**) Calcium carbonate-based fillers (**f**) Dark, non –reflective coating

(**g**) Transparent adhesive/coating (**h**) Adhesive from the previous gluing

Figure 4. Optical microscopy observation of the surface morphology and alteration, illustrating the heterogeneous surface morphology and stratified corrosion layers.

White to off-white fills of variable morphology were identified across both works, with a granular surface texture and diffuse margins consistent with calcium carbonate-based materials applied during late twentieth-century restoration campaigns (Figure 4e). Dark, non-reflective coatings were documented with concentration on the frontal and lateral surfaces, applied preferentially to visually prominent areas, including facial features and torso details. Their distribution pattern and optical behavior—homogeneous appearance, slight surface gloss, absence of UV fluorescence—are consistent with bituminous or wax-based compounds applied to create a bronze-like surface finish (Figure 4f). Multiple bonding sites characterized by glossy, translucent films were identified along crack lines and fracture planes, consistent with synthetic adhesive residues from previous restoration phases (Figure 4g,h).

Optical microscopy documents the coexistence of residual original gilding with bronze powder integrations, copper-based corrosion products, calcium carbonate fills, dark organic coatings, and synthetic adhesive residues, identifying the regions of interest subsequently targeted for compositional analysis.

3.3. Energy-Dispersive X-Ray Fluorescence Spectroscopy (EDXRF)

Portable EDXRF analysis revealed systematic elemental heterogeneity across the surface layers of both sculptures, reflecting the superimposition of original materials and later additions. The locations of all 45 measurement spots are shown in Figures 1 and 2 (see Section 2.2); quantitative results are reported in Table 2.

Measurements acquired on areas macroscopically corresponding to exposed ceramic substrate (analyses 1–6) yielded compositional profiles dominated by silicon (36–44 wt%),

aluminum (12–17 wt%), and iron (11–18 wt%), indicative of a ferruginous, silico-aluminous clay matrix consistent with historical Neapolitan terracotta production from local alluvial and volcanic clay sources [53,54]. These same areas also showed elevated calcium (8–14 wt%) and sulfur (11–12 wt%) concentrations, which are atypical for uncoated clay bodies and are most plausibly attributed to partial penetration of the preparatory layer into the porous ceramic matrix during application [55].

Table 2. EDXRF weight percentages (wt%) of the detected elements, normalized to 100%, for each spectrum. Each value is the mean of three replicate acquisitions. Standard Deviation (SD) < 1.2 wt%.

ID	Category	Al	Si	Ca	S	Fe	Cu	Zn	As	Ag	Au	Pb	Zr
1	Ceramic body	17.79	32.88	9.41	14.29	17.87	0.48	0.17	---	0.35	---	6.76	---
2		17.66	34.94	8.49	15.9	18.19	0.48	0.15	---	0.34	---	3.85	---
3		17.63	34.61	7.65	15.13	18.29	0.48	0.15	---	0.37	---	5.69	---
4		17.56	36.7	8.21	12.41	14.43	0.46	0.33	0.18	---	---	9.72	---
5		16.94	36.73	7.91	12.18	14.16	0.53	0.38	0.19	---	---	10.98	---
6		17.49	36.69	8.21	12.31	11.84	0.52	0.36	0.2	---	---	12.38	---
7	Black patina	0.78	4.18	4.08	2.11	5.07	16.25	0.96	---	---	---	66.57	---
8		0.79	4.21	4.02	2.05	5.09	15.84	1.04	---	---	---	66.96	---
9		0.74	4.06	4.11	2.1	4.2	16.31	0.99	---	---	---	67.49	---
10	Green patina	0.6	3.19	3.09	1.6	3.78	36.44	0.74	---	---	---	50.56	---
11		0.62	2.47	3.04	2.29	3.77	35.73	0.8	---	---	---	51.28	---
12		0.58	3.09	3.12	1.57	3.9	37.06	0.67	---	---	---	50.01	---
13	Original gilding	0.74	2.75	5.94	3.87	6.14	0.41	---	0.72	---	5.05	74.38	---
14		0.73	2.74	5.98	3.95	6.34	0.4	---	0.68	---	5	74.18	---
15		0.71	2.76	6.2	4.16	6.39	0.38	---	0.71	---	4.9	73.79	---
16		1.68	4.55	6.04	3.95	9.33	0.38	---	0.76	---	3.52	69.79	---
17		1.61	4.7	6.14	3.86	9.23	0.39	---	0.73	---	3.62	69.72	---
18		1.72	4.34	6.26	3.99	9.13	0.4	---	0.76	---	3.58	69.82	---
19		0.78	2.99	6.01	3.88	6.72	0.39	---	0.78	---	4.28	74.17	---
20		0.81	3.25	6.29	4.02	7.04	0.42	---	0.78	---	4.23	73.16	---
21		0.78	3.07	5.76	3.8	7.35	0.41	---	0.75	---	4.34	73.74	---
22		1.37	4.18	5.75	3.92	9.16	0.39	---	0.3	---	4.06	70.87	---
23		1.39	4.14	5.97	3.83	9.12	0.4	---	0.31	---	4.11	70.73	---
24		1.46	4.33	6.02	3.85	8.79	0.4	---	0.31	---	4.06	70.78	---
25	Other	2.22	7.63	1.23	---	8.44	1.14	0.14	0.35	0.37	2.96	75.52	---
26		2.36	7.32	1.2	---	7.83	1.06	0.15	0.33	0.35	2.86	76.54	---
27		2.28	7.44	1.24	---	8.07	1.15	0.14	0.35	0.39	2.89	76.05	---
28		0.67	2.71	1.66	---	7.74	0.55	---	0.53	---	2.3	83.84	---
29		0.64	2.71	1.78	---	8.07	0.54	---	0.51	---	2.25	83.5	---
30		0.64	2.78	1.73	---	7.78	0.55	---	0.5	---	2.17	83.85	---
31	*Gesso/ biacca* layer	---	1.13	26.42	23.83	4.2	0.4	---	0.67	---	---	43.23	0.12
32		---	1.22	25.37	25.2	3.98	0.36	---	0.68	---	---	43.07	0.12
33		---	1.12	25.16	23.39	3.92	0.4	---	0.68	---	---	45.21	0.12

Table 2. *Cont.*

ID	Category	Al	Si	Ca	S	Fe	Cu	Zn	As	Ag	Au	Pb	Zr
34	Simulated gilding (*porporina*)	1.16	5.81	3.82	1.04	0.52	6.73	6.17	---	2	---	72.75	---
35		1.23	5.73	4.17	1.03	0.53	6.37	5.85	---	2.08	---	73.01	---
36		1.21	5.95	4.05	1.02	0.52	6.83	6.07	---	2.01	---	72.34	---
37		1.46	4.33	3.85	1.01	0.03	5.57	6.17	---	1.97	---	75.61	---
38		1.45	3.98	3.87	1.04	0.03	5.48	5.86	---	2.11	---	76.18	---
39		1.5	3.95	4.08	0.99	0.03	5.59	6.06	---	1.92	---	75.88	---
40		1.15	4.33	3.95	0.95	0.51	8.67	6.28	---	2.05	---	72.11	---
41		1.2	4.67	3.83	1.05	0.55	7.88	6.16	---	1.92	---	72.74	---
42		1.09	4.63	3.97	1.06	0.52	8.13	6.1	---	1.91	---	72.59	---
43		1.23	4.16	3.86	0.99	0.08	10.22	5.88	---	2.03	---	71.55	---
44		1.29	4.16	3.99	0.94	0.08	9.87	6.32	---	2.11	---	71.24	---
45		1.18	3.93	4.08	1.05	0.08	9.94	5.74	---	1.89	---	72.11	---

Analyses 31–33, corresponding to an exposed plastering or ground layer, confirmed the presence of a stratified preparation system composed predominantly of calcium (25–26 wt%), sulfur (23–25 wt%), and lead (43–45 wt%). This elemental composition is consistent with a ground of calcium sulfate (*gesso*) overlain by a finishing layer (*imprimitura*) of lead white (basic lead carbonate, $2PbCO_3 \cdot Pb(OH)_2$, historically known as *biacca*), applied to provide a smooth, reflective base for subsequent gilding layers [23]. Traces of zirconium (0.12 wt%) detected in these analyses likely originate from natural ceramic inclusions or surface contamination. In areas of preserved original gilding (analyses 13–24), lead remained the dominant element (69–75 wt%), reflecting the analytical depth of EDXRF, which penetrates beyond the thin gold leaf into the underlying lead-rich preparatory layer. Gold concentrations ranged from 3.2 to 5.1 wt%, consistent with the application of an extremely thin gold leaf characteristic of Baroque mission gilding [56].

Iron (6–10 wt%) and calcium (5–6 wt%) were also detected in these areas, indicating the presence of an iron-rich bole layer and residual *gesso* beneath the gilding. Arsenic was detected in most lead-rich areas (0.18–0.78 wt%), likely as a trace component of historical lead or brass alloys.

The black patina areas (analyses 7–9) yielded the most chemically distinctive profiles, characterized by elevated copper (15.8–16.3 wt%), iron (4.2–5.1 wt%), and zinc (0.9–1.0 wt%) in a lead-dominated matrix (66.5–67.5 wt%). This elemental composition is consistent with an artificial patination treatment based on copper salts or complex brass alloys mixed with iron-based pigments, applied to simulate aged bronze surfaces [57,58]. The green patina areas (analyses 10–12) showed similarly elevated copper content (35.7–37.1 wt%) with lower iron, consistent with copper-rich corrosion products. In areas of simulated gilding (analyses 34–45), silver was detected at 1.89–2.11 wt% alongside significant copper (5.5–10.2 wt%) and zinc (5.7–6.3 wt%), consistent with Cu-Zn-Ag alloy powders (*porporina*) applied as metallic powder in a binder medium to reintegrate losses in the original gilding [59,60]. The copper content in these areas is markedly higher than in the original gilded zones, providing a clear analytical criterion for distinguishing the two material categories.

Table 2 reports the elemental composition (expressed as relative weight %) of the different investigated areas on both sculptures. EDXRF analysis discriminates six elementally distinct surface categories: ceramic substrate, *gesso/biacca* preparation, original gilded areas, simulated gilding (*porporina)*, copper-rich black patina, and copper-rich green patina. The elemental signatures are consistent with those reported for Baroque polychrome and gilded

sculpture in Italy and Iberia [28,30,57,58] and define the compositional framework refined by the subsequent Raman, FTIR-ATR, and SEM-EDS analyses.

3.4. Raman Spectroscopy

Raman spectral acquisition on the dark and greenish surface residues (Figure 5) revealed the co-presence of tenorite (CuO) and malachite ($Cu_2CO_3(OH)_2$) within the same measurement areas, indicating a chemically heterogeneous copper-bearing surface layer combining both primary and secondary phases.

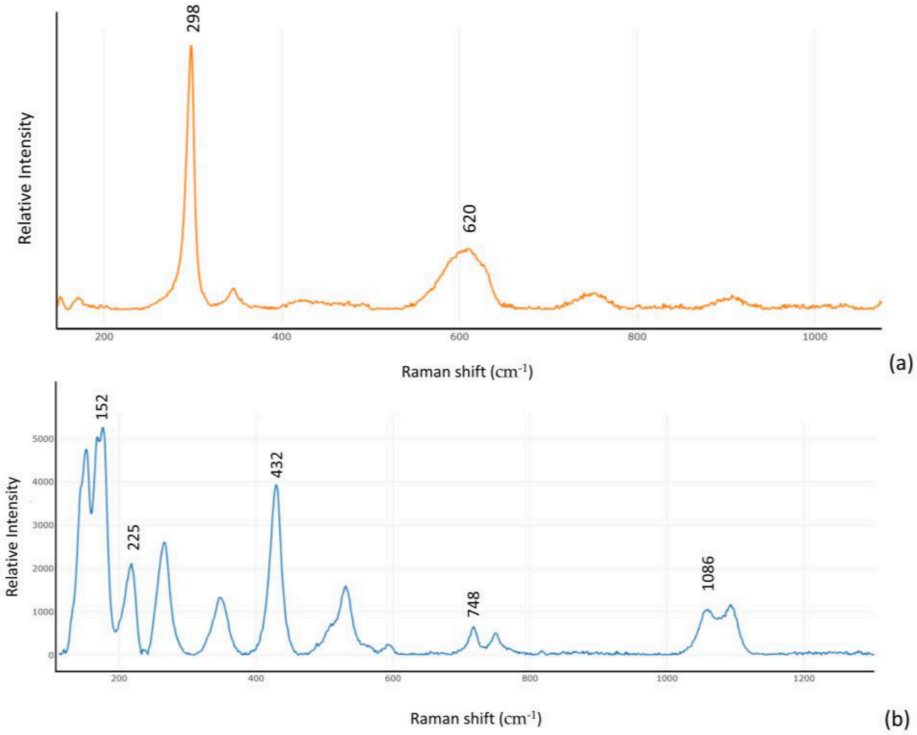

Figure 5. Raman spectrum collected on dark (**a**) and greenish (**b**) surface residue.

Tenorite was identified through characteristic Raman bands at approximately 298 cm^{-1} and 620 cm^{-1} (Figure 5), consistent with the Cu–O stretching modes of black copper (II) oxide. The presence of tenorite as a discrete surface phase is consistent with its intentional application as a patination agent to simulate the appearance of oxidized bronze.

Within the same macroscopic surface zones, bands attributable to malachite were identified at 152, 225, 432, 748, and 1086 cm^{-1}, corresponding to the characteristic vibrational modes of basic copper carbonate. Although individual spectra are dominated by one phase depending on the precise measurement point, the occurrence of both tenorite and malachite within the same surface areas, resolved as discrete spectral signatures at spatially proximate points, indicates a heterogeneous but intimately associated copper-bearing layer in which primary tenorite and secondary malachite coexist at the microscale. This relationship strongly suggests that malachite formed in situ through the progressive carbonation and hydration of tenorite, driven by exposure to atmospheric CO_2 and moisture over time. Contributions from other copper-bearing precursor phases cannot be entirely excluded.

3.5. Fourier Transform Infrared Spectroscopy (FTIR)

FTIR-ATR analysis was performed on eight micro-samples collected from representative surface areas of both sculptures. Sampling locations and material descriptions are provided in Table 3.

Table 3. Sampling spots for FTIR analysis.

Sample ID	Description	Optical Micrograph of the Sampling Area (Scale Bar: 1 mm)
Sample 1	Porporina powder scraped using a micro chisel	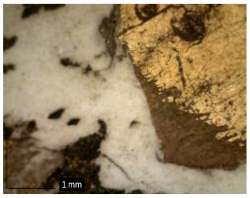
Sample 2	Brown-dark patina covering the gilding	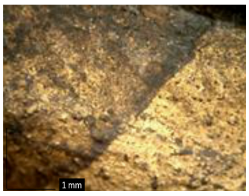
Sample 3	Brown-dark patina covering the gilding	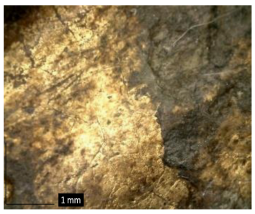
Sample 4	Back, ungilded area covered with black patina	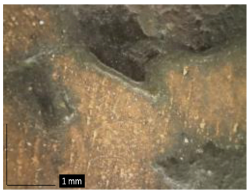
Sample 5	Black patina on hidden drapery area	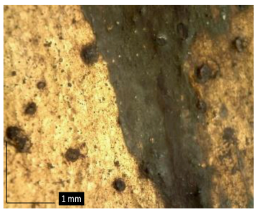
Sample 6	Glue	
Sample 7	Glue	
Sample 8	Synthetic adhesive covering the base	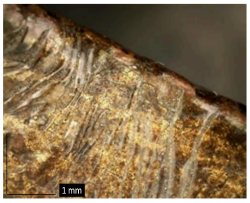

(a) *Sample 1*

Sample 1 (*porporina*-based powder, torso of Hercules B) yielded a spectrum dominated by carbonate absorptions at 1420 cm^{-1} and 875 cm^{-1}, attributable to the asymmetric stretching and out-of-plane bending of the CO_3^{2-} group, consistent with calcium carbonate ($CaCO_3$) [61]. Weak C–H stretching bands between 3000 and 2800 cm^{-1} are present, while the absence of significant absorption in the 1660–1400 cm^{-1} region indicates that organic binders or resinous materials are either absent or present only in trace quantities (Figure 6).

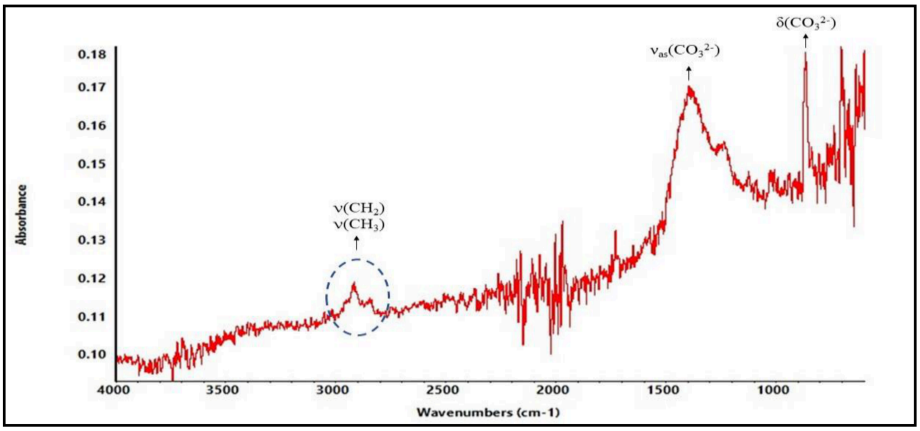

Figure 6. FTIR spectrum of Sample 1.

(b) *Sample 2*

Sample 2 (brown-dark patina on gilded surface, left drapery of Hercules B) showed a complex spectral pattern including: a broad absorption band between 3300 and 3400 cm^{-1} attributable to O-H and N-H stretching vibrations; C–H stretching bands between 2920 and 2850 cm^{-1} indicative of aliphatic hydrocarbon components; Si–O–Si stretching vibrations at 1099, 1043, and 779 cm^{-1}; a carbonyl absorption at 1619 cm^{-1} compatible with ester, carboxylic acid, or altered resin groups; and multiple C–O–C stretching signals between 1200 and 1000 cm^{-1} consistent with degraded natural resins or synthetic polymers (Figure 7). The overall spectral profile is consistent with a complex organic coating containing waxy and bituminous components.

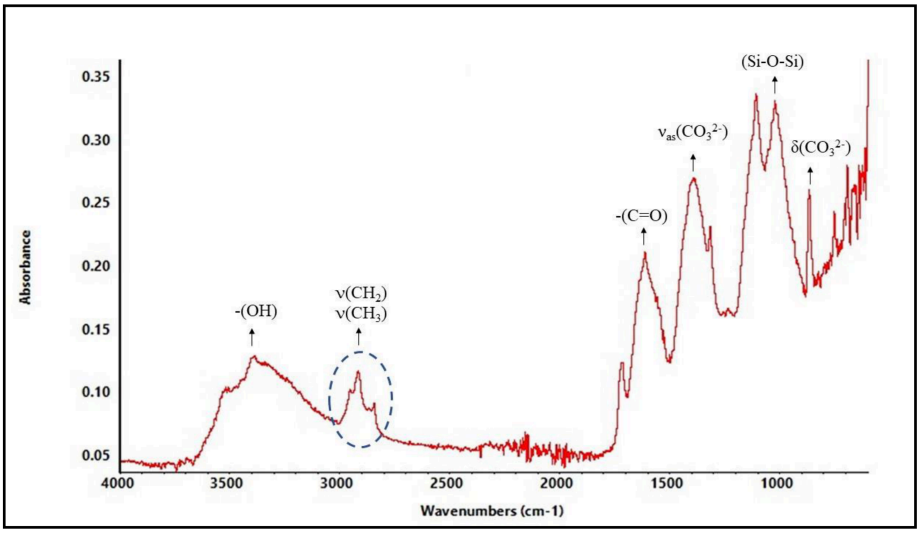

Figure 7. FTIR spectrum related to Sample 2.

(c) *Sample 3*

Sample 3 (brown-dark patina on gilded surface, lion's thigh of Hercules A) yielded an absorbance pattern directly comparable to that of Sample 2, with uniformly more intense bands (Figure 8). These features confirm the presence of waxy and bituminous organic compounds and indicate that a compositionally similar coating was applied to both sculptures.

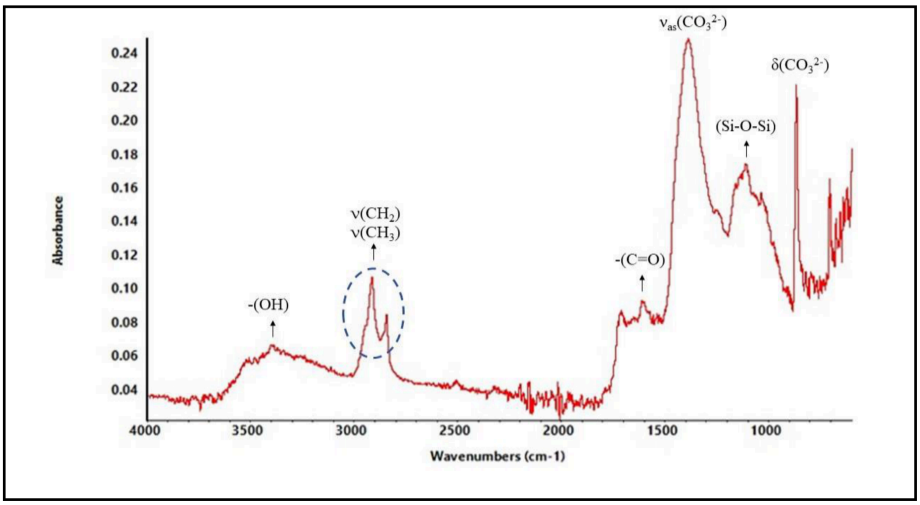

Figure 8. FTIR spectrum related to Sample 3.

(d) *Sample 4*

Sample 4 (black patina on ungilded back area, Hercules B) produced a spectrum consistent with those of Samples 2 and 3 (Figure 9), demonstrating that organic surface compounds of comparable composition were applied across both gilded and ungilded areas, independently of the underlying substrate.

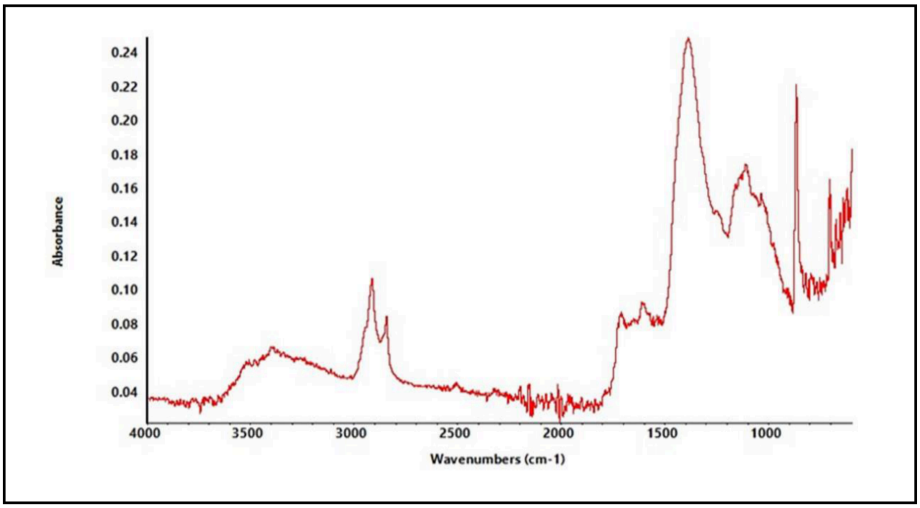

Figure 9. FTIR spectrum related to Sample 4.

(e) *Sample 5*

Sample 5 (black patina on hidden drapery area, Hercules A) showed an absorbance pattern analogous to those of Samples 2, 3, and 4 (Figure 10), indicating that the organic coating was distributed uniformly across both exposed and concealed surface areas of the sculpture. The presence of this material in areas not accessible to casual visual inspection

supports the interpretation of a deliberate, systematic application rather than a selective decorative one.

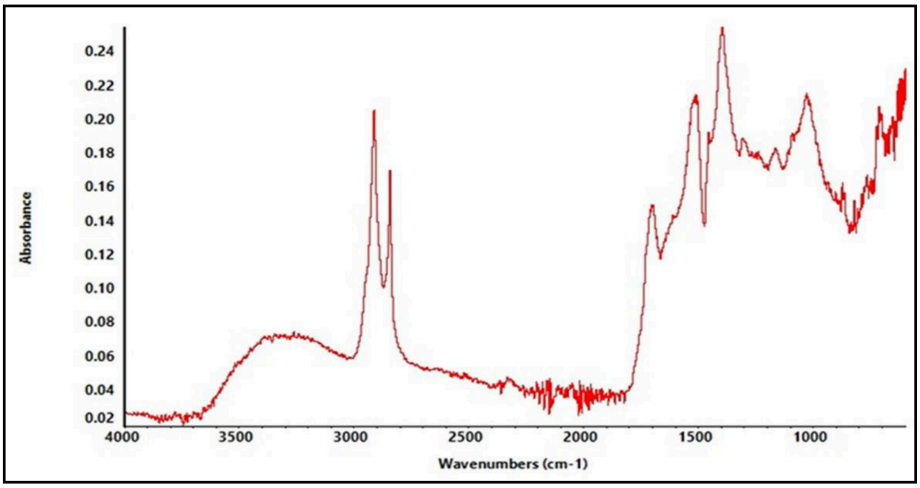

Figure 10. FTIR spectrum related to Sample 5.

(f) *Sample 6*

Sample 6 (glue-like substance, Hercules B surface) revealed the characteristic absorption bands of poly(vinyl acetate) (PVAc): a strong C=O stretching band of ester groups at approximately 1735 cm^{-1}; intense C–O–C stretching absorptions in the 1240–1020 cm^{-1} region; and CH_3 and CH_2 vibrational modes between 2980 and 2850 cm^{-1} (Figure 11). This spectral profile is consistent with a synthetic adhesive based on poly(vinyl acetate), widely employed in twentieth-century conservation treatments of polychrome sculptural artefacts [62].

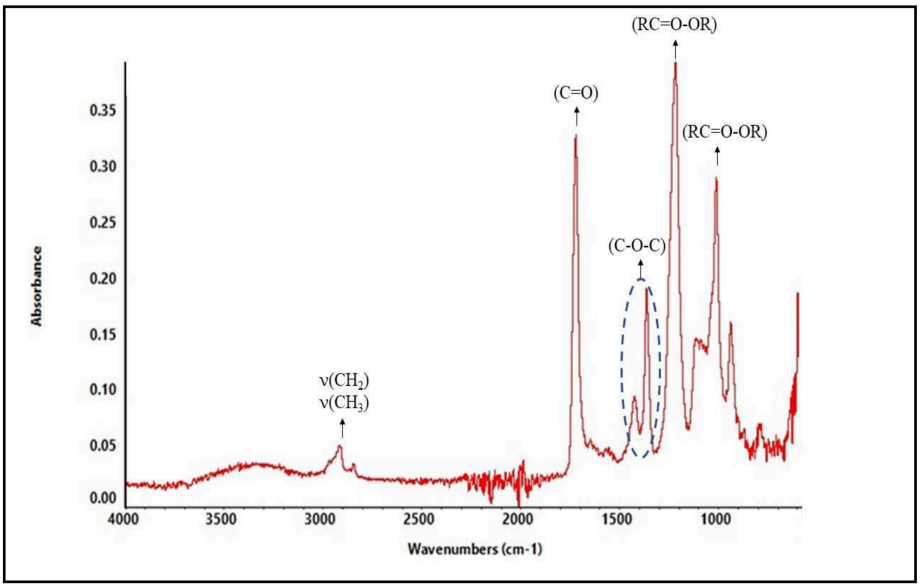

Figure 11. FTIR spectrum related to Sample 6.

(g) *Sample 7*

Sample 7 (glue-like substance, arm of Hercules B) yielded a spectrum identical to that of Sample 6 (Figure 12), confirming the presence of the same poly(vinyl acetate) adhesive on both sculptures.

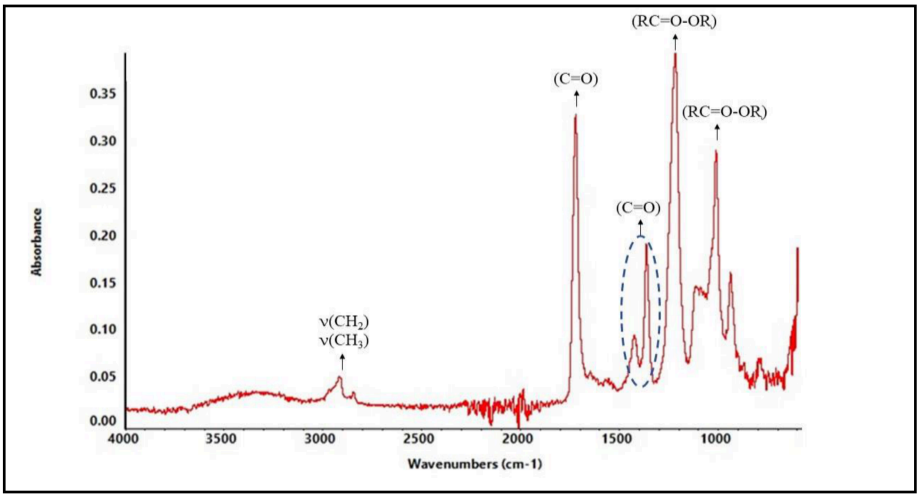

Figure 12. FTIR spectrum related to Sample 7.

(h) *Sample 8*

Sample 8 (transparent film, base of Hercules B) showed absorption bands at 2950–2850 cm^{-1} (CH_3 and CH_2 stretching), approximately 1730 cm^{-1} (ester carbonyl C=O stretching), and 1150–1100 cm^{-1} (C–O stretching) (Figure 13). This spectral pattern is consistent with an acrylic resin or synthetic protective coating, potentially attributable to conservation materials such as Paraloid B-72 or related methacrylate-based copolymers. Its location at the base of the sculpture and the absence of compounds of natural origin suggest a recent application with a protective or consolidating function.

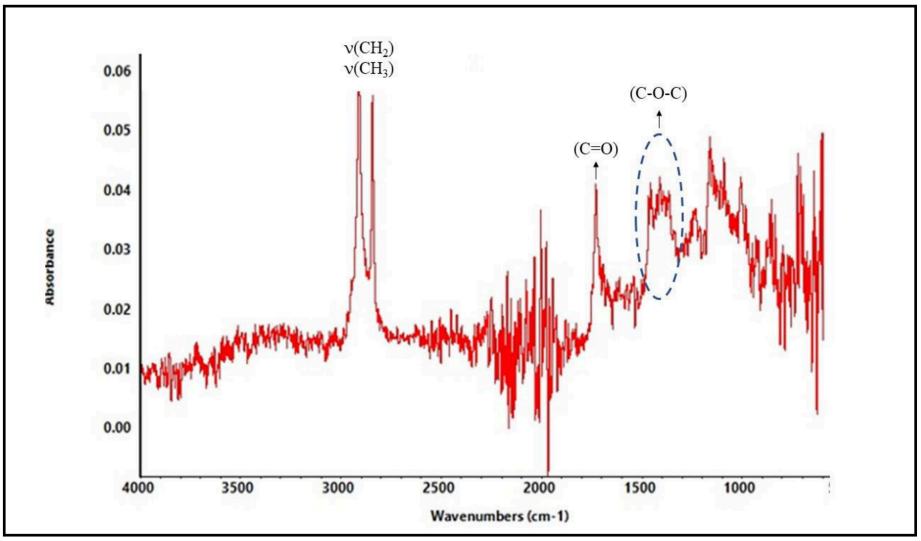

Figure 13. FTIR spectrum related to Sample 8.

The FTIR dataset enables a clear material classification of the surface layers identified on both sculptures, distinguishing four functional categories: mineral preparatory materials (calcium carbonate); organic surface coatings of artificial origin or extensively degraded over time (waxy and bituminous compounds, Samples 2–5); synthetic adhesive binders associated with twentieth-century restoration interventions (poly(vinyl acetate), Samples 6–7); and synthetic protective coatings of recent application (acrylic resin, Sample 8). The full band assignment for all samples is summarized in Table 4.

Table 4. FTIR spectrum showing characteristic absorption peaks attributed to specific functional groups.

Sample	Wavenumber (cm^{-1})	Band Assignment
Sample 1	1420	Asymmetric stretching of carbonate group (CO_3^{2-})
	875	Out-of-plane bending of carbonate group (CO_3^{2-})
	2920–2850	CH_2 and CH_3 stretching
Sample 2	3300–3400 (broad)	–OH or –NH stretching
	2920–2850	CH_2 and CH_3 stretching
	1710–1730	C=O stretching (carbonyl groups)
	1200–1000 (multiple)	C–O stretching
	1086	Si-O-Si stretching
Sample 3	3300–3400 (broad)	–OH or –NH stretching
	2920–2850	CH_2 and CH_3 stretching
	1710–1730	C=O stretching (carbonyl groups)
	1200–1000 (multiple)	C–O stretching
	1086	Si-O-Si stretching
Sample 4	3300–3400 (broad)	–OH or –NH stretching
	2920–2850	CH_2 and CH_3 stretching
	1710–1730	C=O stretching (carbonyl groups)
	1200–1000 (multiple)	C–O stretching
Sample 5	3300–3400 (broad)	–OH or –NH stretching
	2920–2850	CH_2 and CH_3 stretching
	1710–1730	C=O stretching (carbonyl groups)
	1200–1000 (multiple)	C–O stretching
Sample 6	2920–2850	CH_2 and CH_3 stretching
	1735	C=O stretching of ester groups
	1240–1020	C-O-C stretching
Sample 7	2920–2850	CH_2 and CH_3 stretching
	1735	C=O stretching of ester groups
	1240–1020	C-O-C stretching
Sample 8	2950–2850	CH_3 and CH_2 stretching
	1730	C=O stretching (ester)
	1150–1100	C–O stretching

3.6. Scanning Electron Microscopy—Energy Dispersive Spectroscopy (SEM-EDS) Analysis

SEM-EDS analyses were performed on three micro-samples—designated Fragment 1, Fragment 2, and Fragment 3—selected to represent the principal stratigraphic conditions identified on the sculptures. Sampling locations are shown in Figure 2 (see Section 2.2).

1. Fragment 1

Sample 1, named "Fragment 1", was collected from the right side of the base of the Hercules A statue. It was selected as representative among the various broken fragments

in the base. The sample was embedded in resin and examined under a digital optical microscope before SEM analysis.

Microscopic observation (Figure 14) revealed stratigraphy consisting of a dark surface layer with gold-colored inclusions, overlying a continuous and compact ceramic body. The sample exhibits moderate porosity, characteristic of low-fired, iron-rich terracotta, typical of 17th-century Neapolitan production.

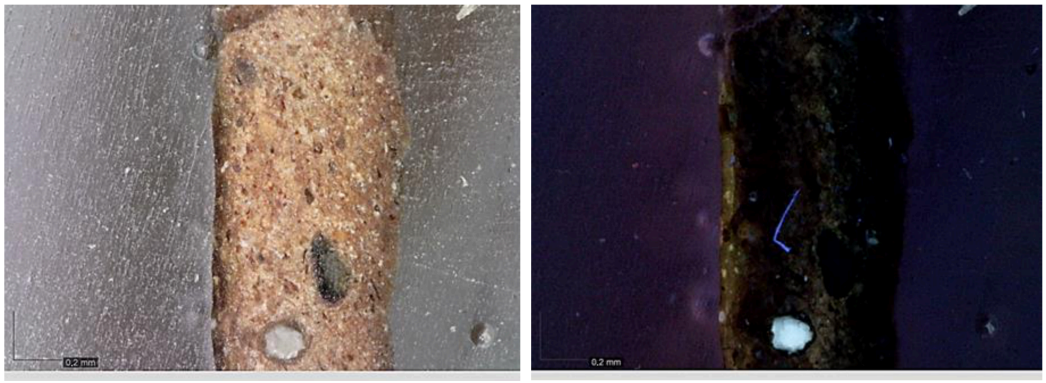

(**a**) (**b**)

Figure 14. Images acquired with a digital optical microscope of Fragment 1 under visible light illumination (**a**) and UV radiation (**b**).

SEM analysis highlighted the presence of three distinct layers within Fragment 1 (Figure 15):

- Surface layer: compact and homogeneous, suggesting a uniform composition.
- Intermediate layer: characterized by white contrasting granules.
- Internal layer: non-homogeneous, containing inclusions, consistent with the ceramic body of the artifact.

EDS analysis of these layers (Table 5) revealed a differentiated elemental distribution, indicative of variations in composition and function among the layers.

Table 5. Quantitative values in wt% (±0.2) of the elements detected with EDS analysis in the areas indicated in the SEM image.

ID	O	Mg	Al	Si	S	K	Ca	Fe	Pb
Spectrum 1	51.3	---	---	---	---	---	6.6	---	42
Spectrum 2	53.5	3.3	8.8	20.9	---	2.0	7.9	3.7	---
Spectrum 3	55.5	---	6.5	29.7	---	3.3	5	---	---
Spectrum 4	45.6	---	8.6	30.5	---	3.0	8.5	3.8	---
Spectrum 5	50.7	---	10.8	22.7	2.4	2.8	8.4	2.2	---

In the outermost layer (Spectra 1 and 2), lead was detected, suggesting the presence of lead-rich preparatory compounds associated with the surface finishing layers, such as gilding.

The intermediate layer (Spectrum 5) contains high-contrast inclusions dominated by zinc and iron, indicating the probable presence of zinc oxide, iron oxides, or other ferriferous phases. Layers 2 and 3 consist predominantly of a clay matrix, likely aluminum silicates (evidenced by the presence of Al and Si) in association with iron oxides.

The contrast difference observed in backscattered electron (BSE) images is likely related to higher silica and iron content in the innermost layer (Spectrum 4). In contrast,

the intermediate layer (Spectrum 5) shows a higher concentration of aluminum, silicon, and oxygen, consistent with alumina-silicate phases, and contains sulfur.

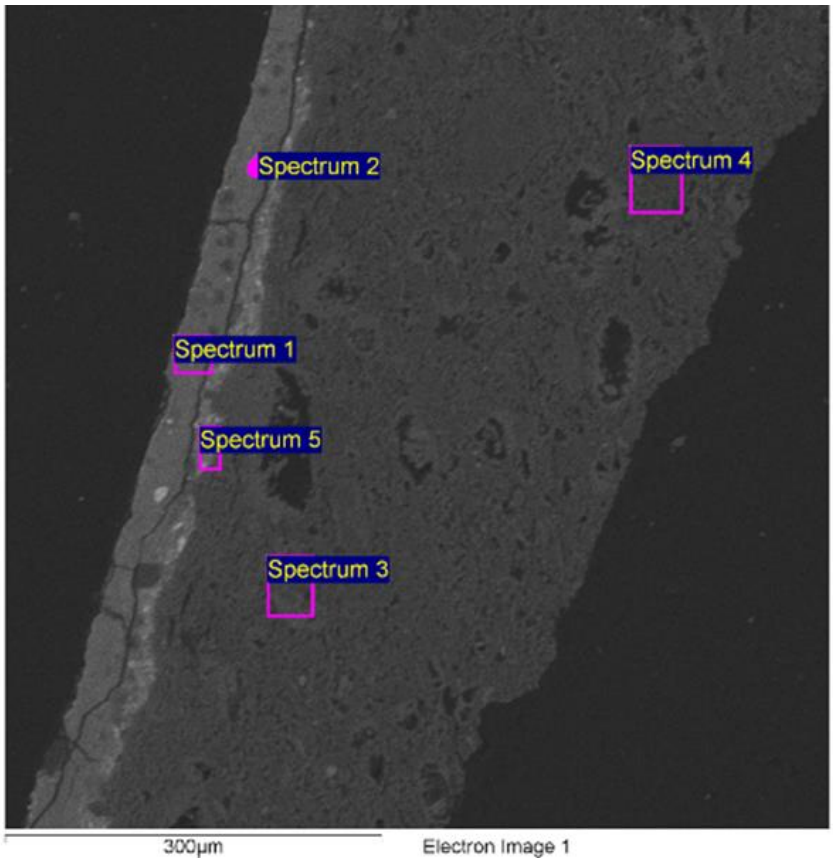

Figure 15. SEM image of Fragment 1 acquired using a BSE detector, showing three distinct layers: (1) outer light grey layer, (2) intermediate light grey layer with white inclusions, and (3) inner dark grey ceramic body. The analyzed areas correspond to the surface layer (layer 1—Spectra 1 and 2), the intermediate layer (layer 2—Spectrum 5), and the internal layer (layer 3—Spectra 3 and 4).

2. Fragment 2

Sample 2, named "Fragment 2," was collected from the back of the lion skin of Hercules statue B, specifically from a protruding fragment previously glued in during the 1980 restoration. Under optical microscopy, the fragment exhibits a brown layer overlaid on the ceramic body (Figure 16).

SEM image of the brown layer confirmed its organic nature. EDS analysis was therefore performed exclusively on the exposed edge at the bottom right (Figure 17 and Table 6).

Table 6. Quantitative elemental composition (wt%, ±0.2) acquired by EDS analysis in the areas indicated in the SEM image.

	O	Mg	Al	Si	K	Ca	Fe
Spectrum 1	55.0	---	---	---	---	2.3	42.7
Spectrum 2	59.5	2.7	7.5	18.1	1.8	8.8	1.6
Spectrum 3	50.5	4.8	---	4.9	---	1.6	38.2
Spectrum 4	58.0	1.8	9.3	25.5	1.5	3.9	---
Spectrum 5	55.2	4.4	7.7	26.1	1.2	5.4	---
Spectrum 6	60.7	---	5.9	26.1	1.2	4.8	1.4

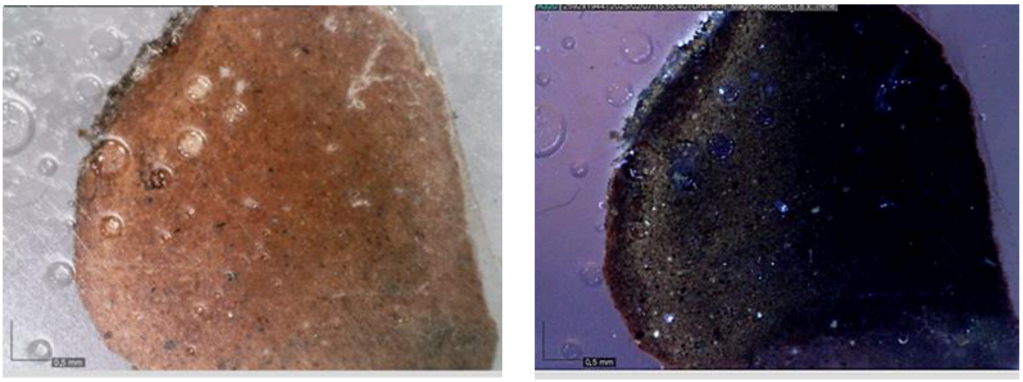

(**a**) (**b**)

Figure 16. Images acquired with a digital optical microscope under visible light (**a**) and ultraviolet radiation (**b**).

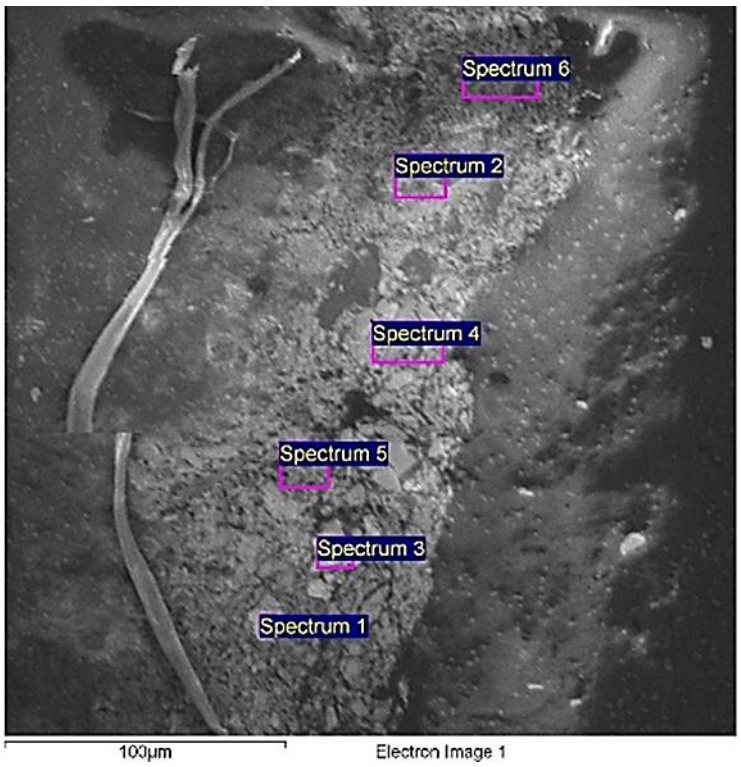

Figure 17. SEM image of Fragment 2 acquired with a BSE detector, showing a thick resin layer and the sample surface on the right side. The analyzed areas are indicated.

Spectra 1 and 3, acquired on two separate inclusions, are primarily composed of iron and oxygen, with smaller amounts of calcium, silicon, and magnesium. This composition is likely attributable to iron oxides, such as hematite (Fe_2O_3), suggesting either the intentional use of ferrous pigments or the natural presence of these oxides in the terracotta matrix. The abundance of iron oxides is consistent with traditional terracotta production techniques, in which hematite contributes the typical red or brown coloration [63].

Other analyzed spectra show a composition dominated mainly by silicon, oxygen, and aluminum, with smaller amounts of iron and significant quantities of calcium, magnesium, and potassium. This elemental distribution indicates the presence of aluminosilicate phases, such as feldspars or kaolin, commonly found in clay matrices used for ceramics and terracotta [64].

3. Fragment 3

"Fragment 3" was collected from the left side of the base of the Hercules B statue. It was selected as representative among the various broken fragments.

Under optical microscopy (Figure 18), Fragment 3 exhibits a complex stratigraphy composed of an outer layer resembling a metal foil, a brown-colored intermediate layer, and an underlying ceramic substrate.

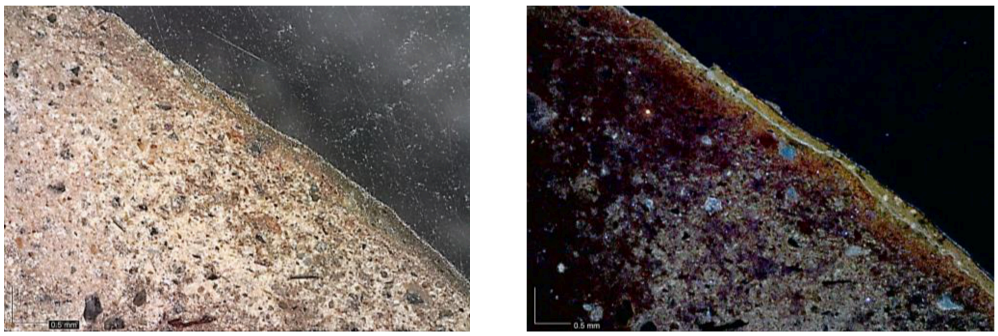

(**a**) (**b**)

Figure 18. Images acquired with a digital optical microscope under visible light (**a**) and ultraviolet radiation (**b**).

SEM images (Figure 19) of Fragment 3 allowed for the identification of four distinct layers, characterized by different elemental contrasts and morphologies:

- Outer layer: The outermost layer, with an estimated thickness of 1.08 µm, appears bright in BSE images, suggesting enrichment in high atomic number elements and indicating the probable presence of a thin metallic layer consistent with gold leaf.
- Compact external layer: Beneath the outer layer, a light gray, compact layer is observed, exhibiting low overall contrast but containing bright inclusions. These inclusions suggest a heterogeneous composition, probably due to the presence of metal oxides.
- Intermediate granular-rich layer: This layer contains bright granules embedded in a light matrix, indicative of compositional heterogeneity, likely associated with metallic oxides.
- Inner layer: The innermost layer corresponds to the ceramic body and exhibits high porosity, suggesting non-uniform firing conditions or the use of clay rich in volatile organic compounds.

EDS analysis revealed detailed compositional information across the layers (Table 7):

Table 7. Quantitative elemental composition (wt%, ±0.2) acquired by EDS analysis in the areas indicated in Figure 19.

	C	O	Mg	Al	Si	S	K	Ca	Fe	Au	Pb
Spectrum 1	---	43.4	---	5.3	16.4	---	4.3	3	2.3	9.4	15.7
Spectrum 2	---	28.7	---	---	---	---	---	---	---	---	71.3
Spectrum 3	---	22.1	---	---	---	---	---	---	---	---	77.8
Spectrum 4	54.1	41.5	---	---	---	---	---	1.7	2.5	---	---
Spectrum 5	46.4	37.2	---	---	---	---	---	---	---	---	16.3
Spectrum 6	---	36	---	---	---	---	---	---	3.4	---	60.5
Spectrum 7	---	49.4	2.6	7.2	24.6	2.1	1.5	10.1	2.5	---	---

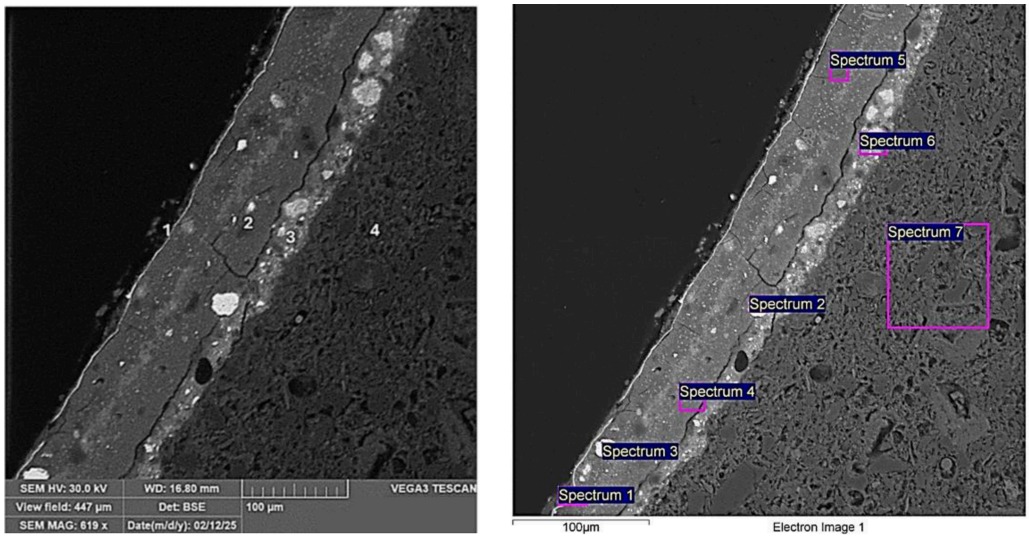

(**a**) (**b**)

Figure 19. SEM image of Fragment 3 acquired with a BSE detector. (**a**): four distinct layers are visible: (1) outer metallic sheet; (2) outer light gray layer; (3) intermediate light gray layer; and (4) inner dark gray ceramic body. (**b**): areas selected for EDS microanalysis are indicated.

At the interface between the outer metallic layer (layer 1) and the underlying layer (layer 2), silicon, aluminum, oxygen, gold, and lead were detected. The localized distribution of gold and silicate phases suggests intentional application as part of a gilding system. The silicate-rich layer is interpreted as a bole layer, traditionally applied to improve the adhesion and optical properties of gold leaf.

Lead is distributed among several layers, most likely originating from the preparatory layers beneath the gold leaf, consistent with past procedures that used lead white ($2PbCO_3 \cdot Pb(OH)_2$) to produce a reflective and smooth base for gilding.

Layers 2 and 3, contain white inclusions, rich in lead and oxygen, compatible with lead-rich compounds derived from alterations in or degradation of lead-based preparatory materials.

EDS analyses of the matrix of the outer layer (Spectra 4 and 5) revealed the presence of iron, calcium, oxygen, carbon, and lead, suggesting the presence of iron oxides, calcium carbonate ($CaCO_3$), and rich compounds.

Taken together, the SEM observations and the EDXRF compositional data indicate a stratigraphic sequence typical of mission gilding on terracotta: a porous ceramic substrate covered by calcium- and lead-rich preparatory layers, followed by an iron-rich bole and a very thin gold leaf. Zinc was additionally detected in several stratigraphic layers at variable concentrations, consistent with either minor additions to the original preparatory mixture or with contribution from overlying restoration materials containing Cu-Zn alloy powders. The calcium- and lead-rich layers detected by EDXRF likely correspond to the *gesso* ground and the lead-white *imprimitura*, which are not always clearly separated in the SEM cross-sections. In several areas, this original structure is further covered by copper-based surface treatments, probably related to later restoration interventions.

Moreover, SEM images and EDS analyses (Figure 20 and Table 8) revealed an additional layer overlying the gold foil. In addition to the elements previously identified in the gold layer, copper was detected, indicating the possible application of a copper-based treatment or a Cu-alloy on the gilded surface. This evidence may be attributable to a protective or decorative intervention carried out after the original gilding process.

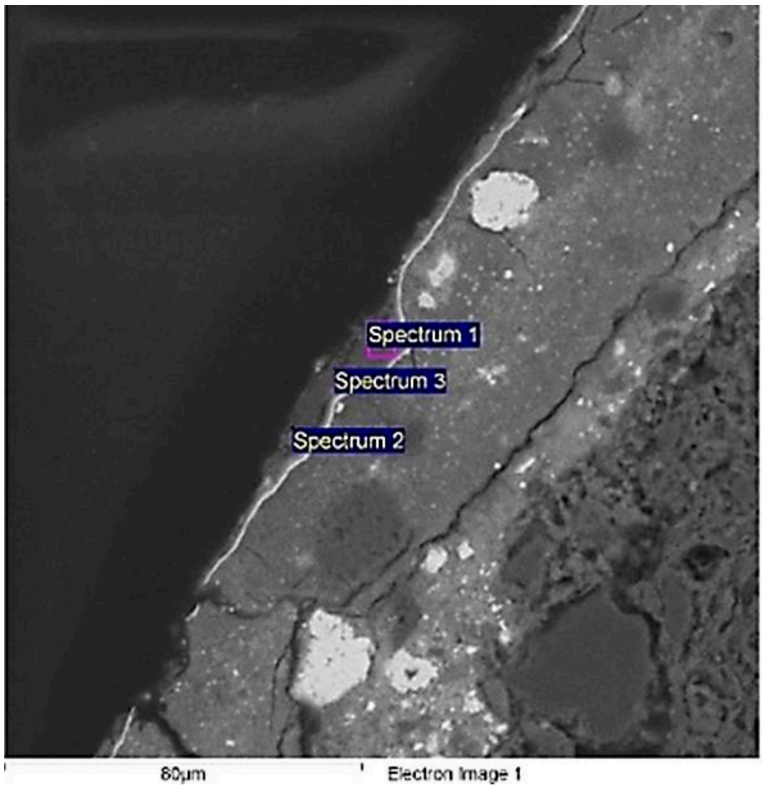

Figure 20. SEM image of Fragment 3 showing the areas analyzed.

Table 8. Quantitative elemental composition (wt%, ±0.2) acquired by EDS analysis in the areas indicated in the SEM image of Figure 20.

	C	O	Na	Mg	Al	Si	K	Ca	Fe	Cu	As	Au	Pb
Spectrum 1	---	50	3.9	---	9.3	26.9	5.8	2.2	1.7	---	---	---	---
Spectrum 2	40.3	29.6	---	---	---	3.0	---	3.4	---	2	---	8.8	12.6
Spectrum 3	---	52.2	---	---	7.6	26.1	4.8	6.5	2.7	---	---	---	--

The combined analysis of the three fragments documents a stratigraphic sequence common to both sculptures, comprising a porous, iron-rich aluminosilicate ceramic substrate, calcium- and lead-rich preparatory layers, an iron-rich bole, and an outer gold leaf. The thickness of the metallic layer, measured on Fragment 3, is approximately 1.08 µm. The bole layer is resolved as a silicate-rich phase enriched in iron and aluminum, in direct contact with the gold leaf. Lead is distributed across multiple stratigraphic levels, consistent with the use of a lead-white finishing layer beneath the gilding. Zinc is detected at variable concentrations in several layers, in association with iron and copper. Copper is additionally identified above the gold leaf in Fragment 3, indicating the presence of a copper-bearing surface treatment superimposed on the original gilded layer. Iron oxides and aluminosilicate phases (feldspars, kaolinitic components) are detected in the ceramic body, consistent with traditional terracotta production.

3.7. Spectrocolorimetry

Spectrocolorimetric measurements were performed on eight selected surface areas of both sculptures, targeting zones representative of the principal material categories identified by the preceding analytical techniques: original gilded surfaces, exposed bole layers, and areas extensively covered by dark patination (Table 9). For each area, measurements were acquired in two contrasting conditions—one on the surface as found, with the overlying

patina intact, and one on the same area following localized removal of the surface deposit—enabling quantification of the chromatic alteration attributable to the patination layers.

Table 9. CIE Lab* colorimetric values measured on selected surface areas under two conditions—surface as found (with overlying patina) and after localized patina removal—together with the calculated total color difference ΔE*ab.

		As Found			After Localized Patina Removal			
Statue	**Area**	**L***	**a***	**b***	**L***	**a***	**b***	**ΔE**
Hercules A	back (gilded)	31.56	6.94	22.91	46.29	7.87	25.28	14.95
Hercules A	lion mane-black patina	16.65	4.09	9.56	46.81	6.90	52.32	52.40
Hercules A	back. red layer (bolo)	15.26	4.83	6.07	18.34	5.75	17.94	12.30
Hercules B	base. frontal view (gilded)	36.74	8.91	23.77	55.14	10.70	34.99	21.63
Hercules B	Hydra head	7.55	4.24	6.07	31.64	9.11	14.61	26.02
Hercules B	back. left side. red layer (bolo)	31.54	10.29	13.95	36.50	13.22	16.97	6.50
Hercules B	back. right side	21.36	1.76	1.99	25.76	6.99	6.13	7.99
Hercules B	back. upper portion. right side	6.35	0.78	1.17	23.87	1.07	1.13	17.52

The total color difference ΔEab between the two conditions ranged from 6.50 to 52.40 across the analyzed areas, with all values substantially exceeding the threshold of visual perceptibility (ΔE < 5). The highest ΔE values were recorded on areas covered by the darkest patination: the lion's mane of Hercules A (ΔE = 52.40, L increasing from 16.65 to 46.81) and the Hydra head of Hercules B (ΔE = 26.02, L* increasing from 7.55 to 31.64), indicating that the overlying deposits had reduced surface brightness by more than 60% relative to the underlying material in the most severely affected zones. On originally gilded areas, ΔE values of 14.95 and 21.63 were recorded for the back of Hercules A and the frontal base of Hercules B, respectively, with corresponding increases in both L* and b* consistent with the recovery of warm golden chromatic values. Areas corresponding to exposed bole showed more moderate ΔE values (6.50–12.30), reflecting the lesser extent of overlying alteration on these surfaces.

The systematic increase in L* across all measured areas confirms (Figure 21) that the surface patination had induced a significant reduction in brightness relative to the original material, while the increase in b* values on gilded and bole areas is consistent with the restoration of warm yellow-red chromatic components characteristic of gold leaf and iron-rich clay, respectively. These data provide quantitative support for the interpretation, based on optical microscopy and spectroscopic analysis, that the dark surface layers represent a superimposed alteration substantially modifying the original chromatic appearance of both sculptures.

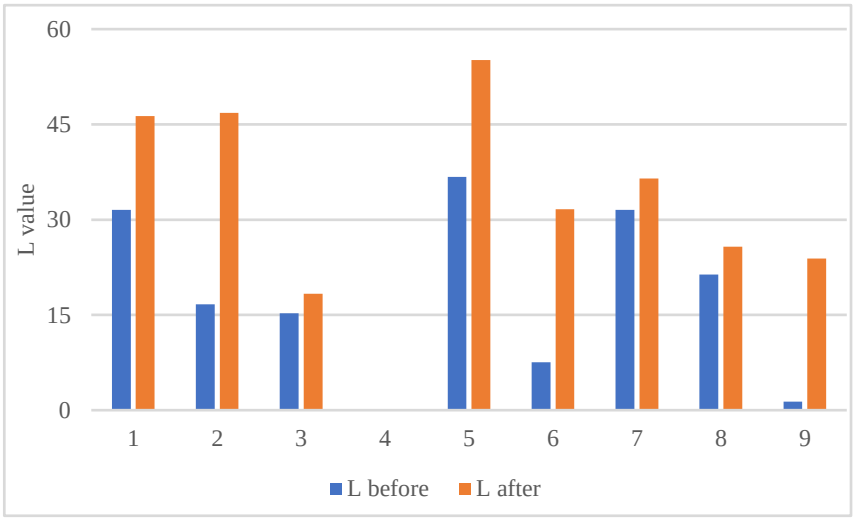

Figure 21. Comparison of L* values measured before and after localized patina removal across the eight analyzed areas.

4. Discussion

The multi-analytical dataset generated in this study allows for a coherent reconstruction of two distinct stratigraphic histories superimposed on the same artworks: the original Baroque gilding system, and the sequence of materials introduced by successive restoration campaigns. Disentangling these two histories—which is the primary scientific challenge in the conservation of gilded terracotta—requires the cross-validation of evidence from complementary techniques, as no single method is sufficient to resolve the full complexity of the surface layers.

The convergent results of EDXRF, SEM-EDS, and optical microscopy define a stratigraphic sequence entirely consistent with the Baroque mission gilding tradition documented for Southern Italian sculpture. The ceramic substrate exhibits a ferruginous silico-aluminous composition (Si 36–44 wt%, Al 12–17 wt%, Fe 11–18 wt%), with moderate iron content accounting for the characteristic reddish coloration observed in cross-section. While elemental composition alone cannot establish clay provenance in the absence of mineralogical phase identification, the documented activity of ceramic workshops in the Campanian region during the seventeenth century, drawing on local alluvial and volcanic clay sources, makes a local provenance historically plausible and consistent with the reported elemental signature [53,54]. Confirmation of this hypothesis would require complementary mineralogical investigation (e.g., X-ray diffraction or petrographic analysis), which lies beyond the scope of the present study. The elevated calcium and sulfur concentrations detected in ceramic-substrate measurements (8–14 wt% Ca; 11–12 wt% S) are atypical for uncoated terracotta and are best explained by infiltration of the preparatory ground into the porous ceramic matrix during application, a phenomenon previously documented in comparable polychrome terracotta sculptures.

The preparatory system itself comprises two compositionally distinct layers identified by both EDXRF and SEM-EDS: a calcium sulfate ground (*gesso*) overlain by a lead-rich finishing layer (*imprimitura* of lead white, $2PbCO_3 \cdot Pb(OH)_2$). The *imprimitura*, evidenced by lead concentrations of 43–45 wt% in ground-layer measurements and confirmed by lead-rich phases in SEM cross-sections, would have provided the smooth, reflective base traditionally required for quality gilding on terracotta. The iron-rich bole layer, detected by EDXRF (Fe 6–10 wt% in gilded areas) and resolved as a distinct silicate-rich phase in SEM-EDS analysis of Fragment 3, is consistent with the use of ferruginous aluminosilicate clays of the type widely employed in Baroque gilding practice.

Gold concentrations of 3.2–5.1 wt% in EDXRF measurements of preserved gilded areas are characteristic of extremely thin gold leaf, whose signal is partially attenuated by the analytical depth of the technique penetrating the underlying lead-rich ground. SEM-EDS examination of Fragment 3 documents a metallic outer layer with an estimated thickness of approximately 1.08 μm, a value within the range reported in the literature for historical gold leaf [12]. This estimate derives from a single cross-section, in line with the operational constraints typical of heritage science investigations on highly fragile gilded surfaces, where micro-sampling for stratigraphic analysis can be ethically justified only on areas already compromised by previous loss. Multiple thickness measurements across different fragments would be desirable to characterize the variability in the gilding application, but were not feasible in the present study. The molecular characterization of the gold leaf alloy itself is also limited by the analytical configuration: the EDS signal of the metallic layer (Fragment 3, Spectrum 2) shows a copper contribution (2 wt%) that cannot be unambiguously attributed to the original alloy composition, given the documented presence of a superimposed copper-based surface treatment whose contribution to the analyzed volume cannot be excluded. Definitive characterization of the alloy, which can provide workshop- and period-level information on gilding practice, would require either dedicated micro-sampling from areas free of the superimposed copper treatment or analytical techniques with higher spatial resolution at the leaf-bole interface, neither of which was applicable in the present study.

Taken together, these data document a technically accomplished and materially coherent gilding system, with each layer fulfilling a specific mechanical or optical function within the overall structure. The molecular characterization of the organic adhesive necessarily present in the original gilding system was not addressed in the present study, as it would have required dedicated micro-sampling from areas of preserved gilding incompatible with the conservation status of the surface. This characterization remains an open question relevant to the planning of future conservation treatments.

The analytical dataset allows for the identification of three distinct, chronologically separated restoration interventions, each characterized by a different combination of materials. The earliest and most pervasive corresponds to the application of a black copper oxide patination intended to transform the visual appearance of the sculptures from gilded to bronze. Tenorite (CuO) identified by Raman spectroscopy, combined with the elevated copper content (15.8–16.3 wt%) in black patina areas detected by EDXRF, constitutes direct evidence of an intentional surface treatment using copper-based compounds. Historical documentation places the removal of most of this patination during the 1978 restoration, when the underlying gilding was rediscovered; however, residual deposits persist in recessed and sheltered areas, as confirmed by the spatial distribution of copper-rich EDXRF analyses and by the UV fluorescence pattern, which shows preferential attenuation on the most visible surfaces. The FTIR identification of waxy and bituminous compounds in Samples 2–5, present on both gilded and ungilded areas, and on both exposed and concealed surfaces, indicates that an organic coating was applied systematically across the entire sculptural surface, independently of the underlying material, further supporting the interpretation of a deliberate patination treatment rather than selective surface protection.

A second, clearly delimited intervention corresponds to the post-1980 earthquake restoration, which introduced bronze powder (*porporina*) integrations, calcium carbonate fills, and poly(vinyl acetate) adhesives. The Cu-Zn-Ag alloy powders identified by EDXRF in simulated gilding areas (Ag 1.89–2.11 wt%; Cu 5.5–10.2 wt%; Zn 5.7–6.3 wt%) are compositionally consistent with the metallic powders used in this period for loss integration. Poly(vinyl acetate), identified by FTIR in Samples 6 and 7, was one of the most widely employed consolidants and adhesives in mid-to-late twentieth-century conservation

practice. A third and more recent intervention is evidenced by Sample 8, whose acrylic resin signature, consistent with Paraloid B-72 or a related methacrylate copolymer, at the base of Hercules B, suggests a later protective or consolidating treatment applied after the *porporina* phase.

The superimposition of these non-original materials on the original gilding system has generated a series of ongoing degradation processes. The most chemically significant is the in situ conversion of tenorite to malachite ($Cu_2CO_3(OH)_2$), demonstrated by the co-presence of both phases within the same surface zones by Raman spectroscopy and corroborated by the elevated copper concentrations detected by EDXRF in the corresponding areas (15.8–16.3 wt% in black patina zones; 35.7–37.1 wt% in green patina zones). This evidence is interpreted as the residual signature of the historical black patination treatment that originally transformed the visual appearance of both sculptures from gilded to bronze-like (linked to documentary evidence of the artificial bronze finish removed during the 1978 rediscovery campaign [40]): the malachite identified today is not a pristine original phase, but the secondary product of the progressive degradation of residual tenorite preserved in recessed and sheltered surface zones.

The mechanism of this transformation is proposed here as a working hypothesis. Progressive carbonation and hydration of CuO in the presence of atmospheric CO_2 and moisture is consistent with the environmental conditions documented for the conservation context and represents a likely contributing pathway. However, the role of organic compounds co-existing on the same surfaces (waxy and bituminous materials identified by FTIR in Samples 2–5, and poly(vinyl acetate) in Samples 6–7) cannot be excluded: organic acids derived from the degradation of these materials are known to participate actively in copper speciation and may contribute to the mobilization and re-precipitation of copper carbonate phases at the surface. Discrimination between purely atmospheric and organic-mediated pathways would require dedicated investigation and lies beyond the scope of the present study.

The volumetric change associated with this mineralogical transformation, combined with the mechanical incompatibility between the rigid copper oxide layer and the flexible gold leaf, is a plausible contributing factor to the microcracking and delamination phenomena documented by optical microscopy.

Additionally, the *porporina* integrations have themselves undergone progressive oxidation, confirmed by photographic documentation showing marked darkening within 10–15 years of application, introducing a further chromatic alteration superimposed on the existing patination. The colorimetric data quantify the cumulative chromatic impact of these alterations: ΔE^*ab values ranging from 6.50 to 52.40 across the analyzed areas demonstrate that the overlying deposits had reduced surface brightness by up to 60% relative to the underlying materials in the most severely affected zones, with the highest values recorded precisely in areas of combined tenorite-malachite patination and *porporina* deposits.

The analytical characterization produced in this study has direct consequences for conservation planning. The clear material differentiation between original gilding layers, gold leaf, iron-rich bole, lead-white *imprimitura*, the *gesso* ground, and superimposed non-original materials provides the necessary scientific basis for evaluating the selectivity of any proposed cleaning treatment. The identification of poly(vinyl acetate) as the principal adhesive in the 1980s restoration is particularly relevant: this material undergoes progressive embrittlement and yellowing with age [65], and its removal requires solvents that must be carefully selected to avoid mobilizing the underlying preparatory layers. The spatial co-occurrence of tenorite and malachite within the same surface zones further complicates any copper-based patination removal strategy, as the two phases respond differently to chemical treatments and their relative proportions vary spatially. The colorimetric dataset provides

a quantitative baseline against which the outcome of future conservation interventions can be objectively evaluated.

5. Conclusions

This study contributes original analytical data on mission-gilded Baroque Neapolitan terracotta, a category of artworks for which systematic scientific documentation remains scarce. The integrated diagnostic framework resolved the original Baroque stratigraphy from the materials introduced by successive restoration campaigns, a distinction unattainable through visual examination or single-technique analysis, providing a material reference point for comparative studies on Southern Italian Baroque gilding.

The identification of the in situ carbonation of intentionally applied tenorite to malachite documents a mechanism by which non-original restoration interventions continue to alter the original gilded surface long after their application. This reframes the conservation problem of historically patinated gilded surfaces as the monitoring of an ongoing reaction rather than the management of static inherited materials. The colorimetric baseline established here (ΔE up to 52) makes such monitoring quantitatively tractable.

The analytical sequence shows that complex polychrome stratigraphies can be resolved within the ethical constraints of museum-context investigation, where micro-sampling must be minimized, and is transferable to comparable gilded terracotta artworks in museum collections.

Author Contributions: Conceptualization, A.M., methodology, A.M., C.Z., T.d.C. and L.P.; validation, I.A.C. and F.V.; formal analysis, A.M.; investigation, A.M., C.Z., I.A.C. and L.P.; data curation, T.d.C., A.M. and F.V.; writing—original draft preparation, A.M. and C.Z.; writing—review and editing, T.d.C. and L.P.; visualization, F.V.; supervision, A.M. All authors have read and agreed to the published version of the manuscript.

Funding: This research received no external funding.

Institutional Review Board Statement: Not applicable.

Informed Consent Statement: Not applicable.

Data Availability Statement: The datasets generated and analyzed during the current study are available from the corresponding author on reasonable request.

Acknowledgments: The authors gratefully acknowledge the Museo Civico Gaetano Filangieri in Naples for granting access to the artworks and for the invaluable support provided throughout this study. Their generous collaboration was essential for the thorough examination and documentation of the gilded terracotta sculptures. The authors further extend their sincere thanks to the Accademia di Belle Arti di Napoli for its continued support of this research. A special and heartfelt acknowledgment is owed to Annamaria Nocera, whose expert supervision of the conservation and restoration work on these remarkable artworks was fundamental to the success of this study. Her dedication, professional rigor, and deep expertise in the treatment of gilded terracotta sculptures have been an indispensable contribution, and the authors are profoundly grateful for her commitment and guidance throughout every phase of the restoration process.

Conflicts of Interest: The authors declare no conflicts of interest.

References and Note

1. Doménech-Carbó, A.; Doménech-Carbó, M.T. Application of instrumental methods in the analysis of historical, artistic, and archaeological objects. In *Electrochemistry for Cultural Heritage. Monographs in Electrochemistry*; Springer: Berlin/Heidelberg, Germany, 2009. [CrossRef]
2. Haddad, A.; Martins, A. Thoroughly modern: Unveiling innovation through material analysis and historical insights. *Herit. Sci.* **2024**, *12*, 393. [CrossRef]

3. Kennedy, C.J.; Penman, M.; Watkinson, D.; Emmerson, N.; Thickett, D.; Bosché, F.; Forster, A.M.; Grau-Bové, J.; Cassar, M. Beyond heritage science: A review. *Heritage* **2024**, *7*, 1510–1538. [CrossRef]
4. Oertel, C.M.; Poduska, K.M. Using heritage materials to inspire new understanding in solid state chemistry. *Chem. Mater.* **2024**, *36*, 9993–10002. [CrossRef]
5. Macchia, A.; de Caro, T.; Colapietro, M.; Carnazza, P. Identification and cleaning of an onion-based residue in a historical layer of Giacomo Balla's Ritratto d'uomo/Eugenio Riva. *Commun. Chem.* **2025**, *8*, 230. [CrossRef]
6. Ma, C.; Dou, H.; Zhao, Z.; Qiu, X.; Li, H.; Wang, X. Review of in-situ non- and micro-destructive techniques for pigment analysis in architectural heritage. *npj Herit. Sci.* **2025**, *13*, 222. [CrossRef]
7. Vettorazzo, C.; Sandström, E.; Troalen, G.L.; Mackay, C.L.; Hulme, N.A. Heritage science applications of ambient mass spectrometry. *Anal. Methods* **2025**, *17*, 3357–3369. [CrossRef] [PubMed]
8. Astolfi, M.L.; Sammartino, M.P. Advances in analytical strategies to study cultural heritage samples—2nd edition. *Molecules* **2025**, *30*, 3952. [CrossRef] [PubMed]
9. Riu, J.; Giussani, B. Analytical chemistry meets art: The transformative role of chemometrics in cultural heritage preservation. *Chemom. Intell. Lab. Syst.* **2024**, *247*, 105095. [CrossRef]
10. Mazzeo, R.; Roda, A.; Prati, S. Analytical chemistry for cultural heritage: A key discipline in conservation research. *Anal. Bioanal. Chem.* **2011**, *399*, 2885–2887. [CrossRef]
11. Badea, E. Chemistry for cultural heritage: Connecting past and future. *Herit. Sci.* **2019**, *7*, 99. [CrossRef]
12. Darque-Ceretti, E.; Felder, E.; Aucouturier, M. Gilding of cultural heritage artefacts: An elaborated technology. *Surf. Eng.* **2013**, *29*, 146–152. [CrossRef]
13. Gulotta, D.; Goidanich, S.; Bertoldi, M.; Bortolotto, S.; Toniolo, L. Gildings and false gildings of the Baroque age: Characterization and conservation problems. *Archaeometry* **2012**, *54*, 940–954. [CrossRef]
14. Sandu, I.C.A.; de Sá, M.H.; Pereira, M.C. Ancient 'gilded' art objects from European cultural heritage: A review on different scales of characterization. *Surf. Interface Anal.* **2011**, *43*, 1134–1151. [CrossRef]
15. Brocchieri, J.; Scialla, E.; Manzone, A.; Oreste, G.; D'Onofrio, A.; Sabbarese, C. An analytical characterization of different gilding techniques on artworks from the Royal Palace (Caserta, Italy). *J. Cult. Herit.* **2022**, *57*, 213–225. [CrossRef]
16. Sarnecka, Z.; Dziki, A. (Eds.) *The Materiality of Terracotta Sculpture in Early Modern Europe*, 1st ed.; Routledge: New York, NY, USA, 2023. [CrossRef]
17. Marinach, C.; Papillon, M.C.; Pepe, C. Identification of binding media in works of art by gas chromatography–mass spectrometry. *J. Cult. Herit.* **2004**, *5*, 231–240. [CrossRef]
18. Pombo Cardoso, I.; Pye, E. Gessoes in Portuguese Baroque gilding grounds, part 1: A study of historical documentary sources. *Stud. Conserv.* **2017**, *62*, 185–209. [CrossRef]
19. Hradil, D.; Hradilová, J.; Bezdička, P.; Serendan, C. Late Gothic/early Renaissance gilding technology and the traditional poliment material "Armenian bole": Truly red clay, or rather bauxite? *Appl. Clay Sci.* **2017**, *135*, 271–281. [CrossRef]
20. Lee, J.S.; Chun, Y.G.; Dong, M.K. Scientific conservation treatment of the gilt-bronze Yoni excavated from Hong Nang Sida Temple in Lao PDR. *J. Conserv. Sci.* **2024**, *40*, 793–803. [CrossRef]
21. Löffler, F. Functional metal-based coatings on ceramic substrates. *Surf. Coat. Technol.* **2000**, *132*, 222–227. [CrossRef]
22. Cession, C. The surface layers of Baroque gildings: Examination, conservation, restoration. *Stud. Conserv.* **1990**, *35*, 33–35. [CrossRef]
23. Pombo Cardoso, I.; Pye, E. Preparing the foundation for stable gilding: Scientific evaluation of the durability of Baroque gesso gilding grounds. *J. Archaeol. Sci.* **2017**, *79*, 86–95. [CrossRef]
24. Gärtner, M. Historical pigments, dyes and binders. *Phys. Sci. Rev.* **2021**, *6*, 419–476. [CrossRef]
25. Darque-Ceretti, E.; Aucouturier, M. Gilding for matter decoration and sublimation. A brief history of the artisanal technical know-how. In Proceedings of the 1st International Conference on Innovation in Art Research and Technology, Evora, Portugal, 10–13 July 2013. Available online: https://minesparis-psl.hal.science/hal-00942768v1 (accessed on 1 October 2025).
26. Figueiredo, E.; Silva, R.J.C.; Araújo, M.F.; Senna-Martinez, J.C. Identification of ancient gilding technology and Late Bronze Age metallurgy by EDXRF, Micro-EDXRF, SEM-EDS and metallographic techniques. *Microchim. Acta* **2010**, *168*, 283–291. [CrossRef]
27. Bu, H.; Zha, J. A methodology for lacquer gilding restoration of sandstone sculptures: A multidisciplinary approach combining material characterization and environmental adaptation. *Coatings* **2025**, *15*, 819. [CrossRef]
28. Colombo, C.; Bracci, S.; Conti, C.; Greco, M.; Realini, M. Non-invasive approach in the study of polychrome terracotta sculptures: Employment of the portable XRF to investigate complex stratigraphy. *X-Ray Spectrom.* **2011**, *40*, 273–279. [CrossRef]
29. Bonizzoni, L.; Galli, A.; Poldi, G. In situ EDXRF analyses on Renaissance plaquettes and indoor bronzes patina problems and provenance clues. *X-Ray Spectrom.* **2008**, *37*, 388–394. [CrossRef]
30. Colombo, C.; Bevilacqua, F.; Brambilla, L.; Conti, C.; Realini, M.; Striova, J.; Zerbi, G. Terracotta polychrome sculptures examined before and after their conservation work: Contributions from non-invasive in situ analytical techniques. *Anal. Bioanal. Chem.* **2011**, *401*, 757–765. [CrossRef]

31. Colombo, C.; Toniolo, L.; Casellato, U. Polychrome terracotta statues of the seventeenth century: Microscopic and spectroscopic characterization. *Stud. Conserv.* **2000**, *45*, 5. [CrossRef]
32. Raditoiu, V.; Chican, I.E.; Raditoiu, A.; Fierascu, I.; Fierascu, R.C.; Fotea, P. Application of Fourier-transform infrared spectroscopy (FTIR) for the study of cultural heritage artifacts. In Proceedings of the VR Technologies in Cultural Heritage, VRTCH 2018, Cham, Switzerland, 3–5 October 2018. [CrossRef]
33. Lazidou, D.; Lampakis, D.; Karapanagiotis, I.; Panayiotou, C. Investigation of the cross-section stratifications of icons using micro-Raman and micro-Fourier transform infrared (FT-IR) spectroscopy. *Appl. Spectrosc.* **2018**, *72*, 1258–1271. [CrossRef] [PubMed]
34. Larson, J. The treatment and examination of painted surfaces on eighteenth-century terracotta sculptures. *Stud. Conserv.* **1990**, *35*, 28–32. [CrossRef]
35. D'Agostino, P. 'Uno stile nuovo': Some little-known models by Lorenzo and Domenico Antonio Vaccaro. In *The Eternal Baroque: Studies in Honour of Jennifer Montagu*; Skira: Milan, Italy, 2015; pp. 333–343.
36. Archivio Storico del Museo Civico Gaetano Filangieri, Naples (ASMCGF). *Filangieri, G. Catalogo del Museo, with Handwritten Additional Inventory (nos. 2773–2993) and Additions to the Library, Interleaved and Annotated Printed Volume*; ASMCGF: Naples, Italy, 1888.
37. Acton, F. *Il Museo Civico Gaetano Filangieri di Napoli. Catalogo Delle Collezioni*; Tipografia Gennaro D'Agostino: Naples, Italy, 1961.
38. De Frutos Sastre, L.M. *El Templo de la Fama: Alegoría del Marqués del Carpio*; Fundación Arte Hispánico: Madrid, Spain, 2009.
39. Archivio di Stato di Napoli (ASN), Notaio Orazio Maria Cretari (ASN, Napoli, Italy). Inventario dei beni mobili di Domenico Antonio Vaccaro, Scheda 161, protocollo 33, ff. 397–399v, con allegati ff. 1–8 al f. 399v. 1745.
40. Causa, R.; Spinosa, N. (Eds.) *Civiltà del '700 a Napoli: 1734–1799, Exhibition Catalogue (Naples, December 1979–October 1980)*; Centro Di: Florence, Italy, 1980; Volume 2.
41. *EN 16085:2012*; Conservation of Cultural Property—Methodology for Sampling from Materials of Cultural Property—General Rules. European Committee for Standardization (CEN): Brussels, Belgium, 2012.
42. *EN 16853:2017*; Conservation of Cultural Heritage—Conservation Process—Decision Making, Planning and Implementation. European Committee for Standardization (CEN): Brussels, Belgium, 2017.
43. Marcos Lanzón, V.; García-Vera, E.; Tenza-Abril, A.J.; De Stefano, V. Use of image analysis to evaluate surface dispersion and covering performance of nanolime coatings sprayed on heritage material substrates. *Appl. Surf. Sci.* **2019**, *480*, 962–968. [CrossRef]
44. de la Rie, R. Fluorescence of paint and varnish layers (part III). *Stud. Conserv.* **1982**, *27*, 102–108. [CrossRef]
45. Cosentino, A. Practical notes on ultraviolet technical photography for art examination. *Conserv. Património* **2015**, *21*, 53–62. [CrossRef]
46. Sandu, I.C.A.; Joosten, I.; Leal, N. Optical imaging applications for the study of cultural heritage artifacts. In *Advances in Laser and Optics Research*; Nova Science Publishers: Hauppauge, NY, USA, 2015; Volume 11, pp. 1–45. Available online: https://novaresearch.unl.pt/en/publications/optical-imaging-applications-for-the-study-of-cultural-heritage-a-2/ (accessed on 2 December 2025).
47. Janssens, K.; Van der Snickt, G.; Vanmeert, F.; Legrand, S.; Nuyts, G.; Alfeld, M.; Monico, L.; Anaf, W.; De Nolf, W.; Vermeulen, M.; et al. Non-invasive and non-destructive examination of artistic pigments, paints, and paintings by means of X-ray methods. In *Analytical Chemistry for Cultural Heritage*; Mazzeo, R., Ed.; Springer: Cham, Switzerland, 2017. [CrossRef]
48. Wu, Q.; Li, Y.; Liang, H. Does substrate colour affect the visual appearance of gilded medieval sculptures? *Herit. Sci.* **2020**, *8*, 63. [CrossRef]
49. Concha-Lozano, N.; Lafon, D.; Sabiri, N.; Gaudon, P. Color thresholds for aesthetically compatible replacement of stones on monuments. *Color Res. Appl.* **2012**, *38*, 356–363. [CrossRef]
50. Burgio, L.; Gregory, T. Protocol for the analysis of cross-sections from gilded surfaces. *Heritage* **2021**, *4*, 2416–2430. [CrossRef]
51. Palladino, N.; Occelli, M.; Wallez, G.; Coquinot, Y.; Lemasson, Q.; Pichon, L.; Stankic, S.; Etgens, V.; Salvant, J. An analytical survey of zinc white historical and modern artists' materials. *Herit. Sci.* **2024**, *12*, 47. [CrossRef]
52. Randazzo, L.; Alberghina, M.F.; La Russa, M.F.; Schiavone, S.; Bianchi, R.; Comello, G.; Milazzo, G.; Cubito, C.; Pantuso, A.; Ricca, M. Two stucco sculptures from the "Salone d'Ercole" in the Racconigi Castle (Cuneo, Italy): A case study. *Case Stud. Constr. Mater.* **2024**, *21*, e03793. [CrossRef]
53. Allocca, F.; Calcaterra, D.; Calicchio, G.; Cappelletti, P.; Colella, A.; Langella, A.; de' Gennaro, M. Ornamental stones in the cultural heritage of Campania region (southern Italy): The Vitulano marbles. In *Natural Stone Resources for Historical Monuments*; The Geological Society of London: London, UK, 2010; Volume 333, pp. 219–231. Available online: https://hdl.handle.net/20.500.12070/8046 (accessed on 1 November 2025).
54. Pelosi, C.; Fodaro, D.; Sforzini, L.; Falcucci, C.; Baraldi, P. The terracotta modelli of Palazzo Venezia in Rome: Investigation of the constituent materials for fundamental knowledge and to aid conservation decisions. *Stud. Conserv.* **2017**, *62*, 266–282. [CrossRef]

55. Sandu, I.; Paba, F.; Murta, E.; Pereira, M.; Ribeiro, C. Travelling beneath the gold surface–Part I: Study and characterization of laboratory reconstructions of Portuguese seventeenth and eighteenth centuries ground and bole layers. *E-Conserv. J.* **2014**, *2*, 95–116. [CrossRef]
56. Sandu, I.C.; Murta, E.; Veiga, R.; Muralha, V.S.; Pereira, M.; Kuckova, S.; Busani, T. An innovative, interdisciplinary, and multi-technique study of gilding and painting techniques in the decoration of the main altarpiece of Miranda do Douro Cathedral (XVII–XVIIIth centuries, Portugal). *Microsc. Res. Tech.* **2013**, *76*, 733–743. [CrossRef] [PubMed]
57. Perez-Rodriguez, J.L.; Robador, M.D.; Haro, M.C.J.d.; Blanes, J.M.M.; Garofano, I.; Odriozola, C.; Duran, A. Non-invasive analytical techniques applied to characterize the components of ancient golden medallions. *Herit. Sci.* **2013**, *1*, 4. [CrossRef]
58. Perez-Rodriguez, J.L.; Robador, M.D.; Albardonedo, A.; Duran, A. Gildings from Andalusia: Materials used in different types of artworks along centuries. *J. Cult. Herit.* **2018**, *31*, 112–121. [CrossRef]
59. Marchetti, A.; Beltran, V.; Storme, P.; Nuyts, G.; Van der Meeren, L.; Skirtach, A.; Otten, E.; Debulpaep, M.; Watteeuw, L.; De Wael, K. All that glitters is not gold: Unraveling the material secrets behind the preservation of historical brass. *J. Cult. Herit.* **2023**, *63*, 179–186. [CrossRef]
60. Salvadò, N.; Buti, S.; Clemente, C.; Beltran, V.; Cinque, G.; Juanhuix, J.; Pradell, T. Microanalytical study of luster glazed gilding and silvering from Baroque altarpieces. *Pure Appl. Chem.* **2018**, *90*, 477–492. [CrossRef]
61. Gunasekaran, S.; Anbalagan, G.; Pandi, S. Raman and infrared spectra of carbonates of calcite structure. *J. Raman Spectrosc.* **2006**, *37*, 892–899. [CrossRef]
62. Moustafa, M.; Abdallah, M.; Abdrabou, A.; Kamal, H.M. A multi-analytical investigation of an ancient Egyptian painted wooden coffin from the Late Period. *Int. J. Conserv. Sci.* **2022**, *13*, 3–14.
63. Dana, K.; Rakib, S.A.; Sinhamahapatra, S. Effect of oxide additives on densification of terracotta. *Appl. Clay Sci.* **2023**, *245*, 107147. [CrossRef]
64. Ion, R.-M.; Fierascu, R.-C.; Teodorescu, S.; Fierascu, I.; Bunghez, I.-R.; Turcanu-Carutiu, D.; Ion, M.-L. Ceramic materials based on clay minerals in cultural heritage study. In *Clays, Clay Minerals and Ceramic Materials Based on Clay Minerals*; InTech: Rijeka, Croatia, 2016. [CrossRef]
65. Novak, M.; Ormsby, B. Poly(vinyl acetate) paints: A literature review of material properties, ageing characteristics, and conservation challenges. *Polymers* **2023**, *15*, 4348. [CrossRef] [PubMed] [PubMed Central]

Disclaimer/Publisher's Note: The statements, opinions and data contained in all publications are solely those of the individual author(s) and contributor(s) and not of MDPI and/or the editor(s). MDPI and/or the editor(s) disclaim responsibility for any injury to people or property resulting from any ideas, methods, instructions or products referred to in the content.